DIPLOMARBEIT

Diagonalization of the Mixed Dynamic Form Factor for mapping orbital information

Ausgeführt am Institut für
Festkörperphysik
der Technischen Universität Wien

Unter der Anleitung von
Ao.Univ.Prof. Dr. Peter Schattschneider
und
Dipl.-Ing. Stefan Löffler
als verantwortlich mitwirkender Assistent

durch
Viktoria Motsch

Dorfstraße 53
2295 Zwerndorf

18. Dezember 2012

Abstract

The mixed dynamic form factor (MDFF) is the key quantity for inelastic scattering of electrons in a crystal. In this work, it is shown how the MDFF can be brought into a diagonal form using matrix diagonalization techniques. In this way the MDFF is transformed to a new basis set, thereby reducing the number of contributing terms in the MDFF. This basis transformation leads to a natural basis which elucidates the underlying physics. It is further shown how to make calculations more accurate by removing several approximations. So far, inelastic scattering models are mainly based on isolated atoms, without taking into account the crystal environment of the material. Therefore the cross-density of states (XDOS) was used to also include crystal field effects. In addition, the dipole approximation was replaced with the fully weighted radial wavefunction overlap. With this improved calculation method, it is possible to make predictions for the direct imaging of atomic orbitals. Finally, simulations were performed on several examples to show its versatility.

Zusammenfassung

Der gemischte dynamische Formfaktor ("mixed dynamic form factor", MDFF) ist essentiell für die Beschreibung von inelastischer Streuung von Elektronen in einem Kristall. In dieser Arbeit wird beschrieben, wie man den MDFF mit Hilfe von Matrixdiagonalisierung in eine diagonale Form bringen kann. Dadurch wird der MDFF in eine neue Basis transformiert, wobei die Anzahl der im MDFF beitragenden Terme reduziert wird. Diese Basistransformation führt das System in eine natürlichere Basis über und liefert dadurch Informationen über die zugrundeliegende Physik. Weiters wird gezeigt, wie man die Berechnung des MDFF präziser machen kann, indem man verschiedene Näherungen entfernt. Bisherige Modelle zur Beschreibung von inelastischer Streuung basieren auf der Annahme isolierter Atomen, ohne dass das kristallographische Umfeld des Materials berücksichtigt wurde. Deshalb wurde die "cross-density of states"(XDOS) verwendet um auch Kristallfeldeffekte zu berücksichtigen. Zusätzlich wurde die Dipolnäherung mit dem gewichteten radialen Wellenfunktionsüberlapp ersetzt. Mit dieser verbesserten Rechenmethode ist es möglich, Vorhersagen über das direkte Abbilden von Atomorbitalen zu treffen. Um die Vielseitigkeit der Methode zu zeigen, wurden Simulationen für verschiedene Beispiele gerechnet.

Danksagung

Ich möchte mich bei Prof. Peter Schattschneider für die Unterstützung und Betreuung meiner Diplomarbeit sehr herzlich bedanken. Er hat mir die Möglichkeit gegeben, meine Arbeit bei Konferenzen zu präsentieren, wo ich wertvolle Erfahrungen sammeln konnte.

Mein besonderer Dank gilt Stefan Löffler. Er hatte immer ein offenes Ohr für Fragen und eine Engelsgeduld. Von seinem umfangreichen Wissen bezüglich Elektronenstreuung habe ich sehr profitiert, ebenso brachte er mir viel praktisches Wissen im Umgang mit Linux und LaTeX bei. Ohne ihn wäre diese Arbeit nicht das, was sie geworden ist.

Ich möchte mich bei Walid Hetaba bedanken, dass er mich zur Elektronenmikroskopie geführt hat, ohne ihn wäre ich nicht zu dieser tollen Gruppe gestoßen. Er stand mir immer mit Rat und Tat zur Seite, vor allem mit seinem Wissen über Wien2k.

Außerdem möchte ich mich beim FWF (Fonds zur Förderung der wissenschaftlichen Forschung) für die Forschungsbeihilfe unter der Projektnummer I543-N20 bedanken.

Mein vielleicht größter Dank gilt meinen Eltern. Sie haben mich während des gesamten Studiums sowie auch schon davor unterstützt. Sie gaben mir ein Umfeld in dem ich mich voll und ganz auf mein Studium konzentrieren konnte, fieberten bei allen Prüfungen mit und waren immer für mich da.

Mein Cousin Michael war ein ständiger Wegbegleiter meines Studiums und stand mir immer mit Rat und Tat zur Seite. Durch ihn habe ich viele wertvolle Erfahrungen gesammelt. Dafür möchte ich mich bei ihm herzlich bedanken.

Zum Abschluss möchte ich mich bei meinem Freund Christian für seine Unterstützung bedanken sowie bei allen Freunden und Kollegen für die schöne gemeinsame Zeit.

Contents

List of Figures

List of Tables

List of Abbreviations

DOS	Density Of States
EELS	Electron Energy Loss Spectrometry
EFTEM	Energy Filtered Transmission Electron Microscopy
ELNES	Energy Loss Near Edge Structure
MDFF	Mixed Dynamic Form Factor
pDOS	partial Density Of States
rMDFF	real-space Mixed Dynamic Form Factor
TEM	Transmission Electron Microscope
WRWO	Weighted Radial Wavefunction Overlap
XDOS	Cross Density Of States

Chapter 1

Introduction

1.1 Aim of this thesis

The MDFF is the key quantity in order to describe the inelastic scattering of electrons in a crystal. [1–3] It is crucial for image simulations in order to plan and understand experiments with a transmission electron microscope (TEM). So far inelastic scattering models were based on the dipole approximation but recently it has been shown that this approximation can lead to severe errors. [2] Therefore, the fully weighted radial wavefunction overlap was used to perform accurate calculations. Further, instead of looking at an isolated atom, crystal field effects were also taken into account and the cross density of states (XDOS) was included. Beside of making simulations more exact, the aim of this thesis was to find the most suitable basis set to describe a system: a basis which provides us with more physical insight into the problem and a simpler mathematical description of the system. Conventionally, the MDFF is given in a Y_l^m-basis. In this representation, many of the off-diagonal matrix elements can be non-zero which describe correlation effects. Performing a basis transformation in such a way that the MDFF is diagonal in the new basis, reduces the number of terms and leads to a simpler and natural description of the system. With recent advances of aberration corrected microscopes, improved simulation techniques gain more and more importance and it is even possible to make predictions for the direct imaging of atomic orbitals as will be shown below.

In the first part of this thesis I will explain the theoretical description of the diagonalization of the MDFF. The different steps needed for the implementation of this procedure are shown in the second chapter. Finally, simulations for two different sample materials were performed.

1.2 The Transmission Electron Microscope

The investigation and characterization of materials on the nanoscale became of particular interest in the 20th century. The development of the transmission electron microscope (TEM) by Ernst Ruska in 1936 [3] provided a very useful but also expensive tool for this analysis. In addition to imaging, a broad range of characterization techniques with high spatial and analytical resolution is possible with this instrument. [4] Nowadays, the TEM is widely used in different scientific fields, e.g. material science, biology and life science. This section gives a brief overview of the structure of the TEM and of electron energy loss spectrometry (EELS) as well as energy filtered TEM (EFTEM), two particular analytical techniques which are available in the instrument. [5]

1.2.1 The structure of the TEM

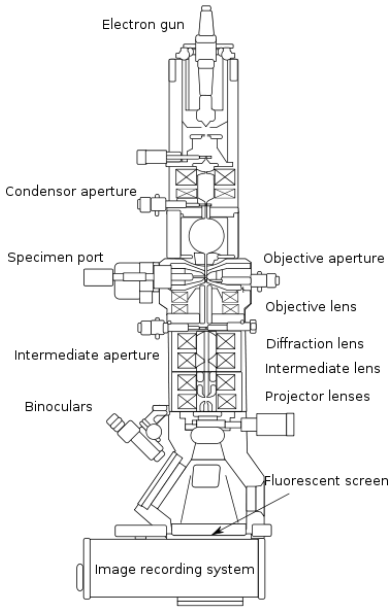

Figure 1.1: Schematic sketch of a TEM. [6]

In a TEM electrons are accelerated at a high voltage (typically 60 – 300 kV) and directed at the target. After interaction with the specimen, the transmitted electrons are detected and analysed. Electrons are used as a probe for several reasons. According to the Rayleigh criterion, also called the Abbe diffraction limit, the minimum distance between two resolvable points is directly proportional to the wavelength of the incoming particle. [3] Then it follows, that due to their extremely short wavelength in the range of picometer (at typical acceleration voltages), electrons can

overcome the limited image resolution of light microscopes. Further, they can easily be manipulated by deflecting their trajectories in the field of magnetic lenses because they are charged particles. How this is done by lenses in the microscope is schematically seen in figure 1.1. The electron source is normally located at the top of the TEM. The illumination system, consisting of several lenses, e.g. gun lenses, condensor lenses, etc. guides the electrons to the specimen and forms the beam. It is usually operated either in parallel-beam or in convergent-beam mode. The next part which the beam passes through is the imaging system located at the position of the specimen holder. It consists of the objective lens, which forms images and — at the backfocal plane — diffraction patterns. Then, the electrons pass through the projector lenses to a fluorescent screen, a CCD camera or other attached devices. All basic operations in a TEM are controlled by the electromagnetic lenses. Therefore it is important to understand electron lenses and their aberrations. Electron lenses are the equivalent to glass lenses in a visible light microscope (VLM) and all lenses in a standard TEM can be compared to convex glass lenses for monochromatic light. But compared to glass lenses in a VLM, it is considerably harder to correct lens errors for electron lenses and lens errors limit the resolution rather than the wavelength. Further, as the collection angle is limited by inserting apertures in the optical path, not all rays from the object are collected. The three major problems in electromagnetic lenses are spherical aberration (C_S), chromatic aberration[1] (C_C) and astigmatism. Spherical aberration means that rays that pass through the central region of a lens are focused farther away than off-axis rays. Nowadays it is possible to use C_S-corrected TEMs, e.g. the FEI Titan G2 60-300. Chromatic aberration means that electrons with a lower energy are bent differently depending on their energy. This affects in particular the objectiv lens as the electron energy can be widely distributed after interaction with the specimen. Astigmatism appears if the electrons pass a non-uniform magnetic field but can be corrected easily nowadays. Lens errors can be reduced, in general, by inserting a limiting aperture such that only the electron rays nearest to the optical axis contribute. Image simulation is used to compare calculated images with results from actual experiments and consequently understand experimental images. For an adequate comparison, it is therefore necessary to include lens errors in the simulation. [5]

1.2.2 EELS and EFTEM

Electron energy loss spectrometry (EELS) is a very powerful analytical technique to identify and quantify the different elements occurring in the sample and to obtain information on the electronic structure of the target. Fast elec-

[1] For monochromatic light, which is light of just one color with an extremly narrow wavelength range, chromatic abberation has no effect.

trons are interacting in different ways with the specimen, varying from no interaction at all, over elastic scattering to inelastic scattering. The energy distribution of these electrons is measured, commonly by using a magnetic prism spectrometer, and the probability of an interaction as a function of the energy loss is called electron energy loss spectrum. Edges above ~ 50 eV (core losses) in the spectrum indicate ionization processes, they can be used to identify different elements. But also other excitations like phonons, plasmons and interband transition contribute to the spectrum. If only electrons which have lost[2] a specific energy are selected to form an image, it is called an energy filtered TEM (EFTEM) image. Using this technique, chemical mapping can be performed with high spatial resolution. [4]

1.3 Theoretical Background

Image simulation is crucial for planning and interpreting TEM experiments and especially EFTEM measurements. The multislice approach [7, 8] is a state of the art method for the real-space simulation of scattering effects of fast electrons in crystals. So far, inelastic scattering models are mainly based on isolated atoms, without taking into account the crystal environment of the material. Moreover, the dipole approximation is typically used for calculating the radial wavefunction overlap. In order to get a deeper theoretical understanding of such experiments, more realistic calculations are needed.

In this section, I will introduce the MDFF and provide the theoretical background to understand the simulation process. First, I will show how the MDFF can be described in the density matrix formalism [9] and why this formalism is needed. It is shown how the additional information on the system which was not taken into account so far, i.e. the crystal field and the fully weighted radial wavefunction overlap, are included. Then, I will analyse the basis transformation which reduces the numerical complexity of the problem. Further, I will explain the physical significance of this procedure.

1.3.1 Density matrix formalism

If a quantum mechanical system is in a pure state, it is maximally characterized with respect to commuting observables and can be described by a single-state vector $|\psi\rangle$. [10] In contrast, a system is said to be a statistical mixture if it has certain propabilities p_1, p_2, ... to be in the pure states $|\psi_1\rangle$, $|\psi_2\rangle$, ... Then, it cannot be written as a single-state vector and is therefore called a mixed state. The density operator can be used as a quantum

[2] Of course, energy cannot be lost and the total amount of energy in the system is conserved. So if electrons lose a certain amount of energy it is transfered to the specimen.

mechanical tool to describe the system, regardless if it is in a pure or in a mixed state. The density operator is defined as

$$\hat{\boldsymbol{\rho}} = \sum_k p_k |\psi_k\rangle\langle\psi_k| \tag{1.1}$$

where p_k is the probability that the system is in the quantum mechanical state $|\psi_k\rangle$. Whereas the single state $|\psi_k\rangle$ can be considered as a coherent superposition of basis states $\{|\phi\rangle\}$, the total system is an incoherent superposition of single states $|\psi_k\rangle$. The vectors $|\psi\rangle$ and $e^{i\phi}|\psi\rangle$ which characterize the same physical state with a different phase, are represented by the same density operator. Therefore, using the density operator, the global phase gets surpressed. The matrix representation of the density operator in a certain basis is called the density matrix, e.g. in plane waves representation $\{|\boldsymbol{k}\rangle\}$ the density matrix is $\rho(\mathbf{k}, \mathbf{k}') = \langle\mathbf{k}|\hat{\boldsymbol{\rho}}|\mathbf{k}'\rangle$. The diagonal elements of this density matrix $\rho(\mathbf{k}, \mathbf{k})$ describe the occupation of the according state, whereas the off diagonal elements $\rho(\mathbf{k}, \mathbf{k}')$, arising from the coherent superposition, describe interference effects between different basis states. [10, 11]

In case of a TEM, the quantum mechanical system consists of the probe electron and the target. After interaction, these two subsystem cannot be disentangled as the target's final state is not directly observed. In this case, if one of the two subsystems cannot be measured, it is not possible to describe the second subsystem with a single state vector and the obtainable information can be most generally described with the density operator approach. [10] Therefore this approach is necessary and the simpler wavefunction description cannot be used.

I assume that, before a perturbation or interaction, the probe and the target are independent and can be described by a pure state. Therefore, the whole system can be written as a product state of the wavefunctions of the probe and the target:

$$|\psi_i\rangle = |i\rangle \otimes |I\rangle. \tag{1.2}$$

Throughout this thesis, lower case letters are related to the probe state and upper case letters to the target state. $\otimes$ denotes the direct product. In this description, the probe and the target state are considered independent. The density operator, in absence of an interaction V, then reads

$$\hat{\boldsymbol{\rho}}_{tot,0} = |\psi_i\rangle\langle\psi_i| = |i\rangle\langle i| \otimes |I\rangle\langle I| = |I\rangle|i\rangle\langle i|\langle I|. \tag{1.3}$$

In first order Born approximation scattering by an extended body can be replaced with a single scattering event if the energy of the scattered particle is large compared to the scattering potential. In this approximation, the density operator of the whole system after an interaction V is[3]

$$\hat{\boldsymbol{\rho}}_{tot} = \hat{V}|I\rangle|i\rangle\langle i|\langle I|\hat{V}^\dagger\delta(E_I - E_F + E). \tag{1.4}$$

[3] This equation can be rigorously derived using the Lippmann-Schwinger equation, which gives rise to the delta distribution in energy. Formally, the scattering matrix in first order Born approximation gives the same result.

For our ignorance of the target system, as it cannot be directly observed, it is necessary to sum incoherently over all possible final states to construct the (reduced) density operator for the probe beam after the interaction. Further, the scattering processes at different scattering centers of the target are not correlated, as the initial states are tightly bound and therefore uncorrelated. Hence, the density matrix formalism is very utile to include incoherent superposition. After the interaction, the electron beam is an incoherent mixture of states and accordingly the reduced density operator then describes a mixed state:

$$\hat{\boldsymbol{\rho}} = \sum_F \langle F|\hat{V}|I\rangle|i\rangle\langle i|\langle I|\hat{V}^\dagger|F\rangle\delta(E_I - E_F + E). \tag{1.5}$$

In EELS experiments, the interaction between charged particles is observed. Therefore, the Coulomb interaction operator[4] is used as the interaction operator. In real space representation, neglecting constant prefactors, it reads

$$\begin{aligned} V(\mathbf{r},\mathbf{r}') = \langle \mathbf{r}|\hat{V}|\mathbf{r}'\rangle &= \frac{1}{|\mathbf{r}-\hat{\mathbf{R}}|}\delta(\hat{\mathbf{R}}-\hat{\mathbf{R}}')\delta(\mathbf{r}-\mathbf{r}') \\ &= \hat{V}(\mathbf{r})\delta(\mathbf{r}-\mathbf{r}'). \end{aligned} \tag{1.6}$$

After Fourier transformation, the interaction operator in reciprocal space is

$$\begin{aligned} \hat{V}(\mathbf{k},\mathbf{k}') = \langle \mathbf{k}|\hat{V}|\mathbf{k}'\rangle &= \frac{e^{i(\mathbf{k}'-\mathbf{k})\hat{\mathbf{R}}}}{|\mathbf{k}'-\mathbf{k}|^2}\delta(\hat{\mathbf{R}}-\hat{\mathbf{R}}') \\ &= \frac{e^{i\mathbf{q}\hat{\mathbf{R}}}}{|\mathbf{q}|^2}\delta(\hat{\mathbf{R}}-\hat{\mathbf{R}}') \\ &= \hat{V}(\mathbf{q}) \end{aligned} \tag{1.7}$$

with

$$\mathbf{q} = \mathbf{k}' - \mathbf{k}. \tag{1.8}$$

$\mathbf{q}$ is the scattering vector describing the momentum transfer. E denotes the energy loss of the probe electron and E_I, E_F are the energies of the targets initial and final states. The energy loss E can also be seen as the energy difference $E_i - E_f$ between the probe's initial states:

$$E = E_i - E_f = E_F - E_I. \tag{1.9}$$

Using the completeness relation

$$\int \mathrm{d}\tilde{\mathbf{r}}|\tilde{\mathbf{r}}\rangle\langle\tilde{\mathbf{r}}| = \mathbb{1} \tag{1.10}$$

[4]In fact, the Coulomb interaction has infinte range, but due to the presence of mobile charge carriers the electric field is damped at larger distances and an affectively limited potential can be assumed.

the reduced density matrix in real space and in reciprocal space reads

$$\begin{aligned}\rho(\mathbf{r},\mathbf{r}') = \langle\mathbf{r}|\hat{\boldsymbol{\rho}}|\mathbf{r}'\rangle &= \sum_F \int \mathrm{d}\tilde{\mathbf{r}}\langle F|\langle\mathbf{r}|\hat{V}|\tilde{\mathbf{r}}\rangle|I\rangle\langle\tilde{\mathbf{r}}|i\rangle \\ &\int \mathrm{d}\tilde{\mathbf{r}}'\langle i|\tilde{\mathbf{r}}'\rangle\langle I|\langle\tilde{\mathbf{r}}'|\hat{V}^\dagger|\mathbf{r}'\rangle|F\rangle\delta(E_I - E_F + E) \\ &= \sum_F \langle F|\hat{V}(\mathbf{r})|I\rangle\langle I|\hat{V}^\dagger(\mathbf{r}')|F\rangle\delta(E_I - E_F + E)\langle\mathbf{r}|i\rangle\langle i|\mathbf{r}'\rangle \\ &= S(\mathbf{r},\mathbf{r}')\langle\mathbf{r}|i\rangle\langle i|\mathbf{r}'\rangle\end{aligned} \tag{1.11}$$

$$\begin{aligned}\rho(\mathbf{k},\mathbf{k}') = \langle\mathbf{k}|\hat{\boldsymbol{\rho}}|\mathbf{k}'\rangle &= \sum_F \int \mathrm{d}\tilde{\mathbf{k}}\langle F|\langle\mathbf{k}|\hat{V}|\tilde{\mathbf{k}}\rangle|I\rangle\langle\tilde{\mathbf{k}}|i\rangle \\ &\int \mathrm{d}\tilde{\mathbf{k}}'\langle i|\tilde{\mathbf{k}}'\rangle\langle I|\langle\tilde{\mathbf{k}}'|\hat{V}^\dagger|\mathbf{k}'\rangle|F\rangle\delta(E_I - E_F + E) \\ &= \sum_F \int\int \mathrm{d}\mathbf{q}\mathrm{d}\mathbf{q}'\langle F|\hat{V}(\mathbf{q})|I\rangle\langle I|\hat{V}^\dagger(\mathbf{q}')|F\rangle \\ &\delta(E_I - E_F + E)\langle\mathbf{k}+\mathbf{q}|i\rangle\langle i|\mathbf{k}'+\mathbf{q}'\rangle \\ &= \int\int \mathrm{d}\mathbf{q}\mathrm{d}\mathbf{q}' S(\mathbf{q},\mathbf{q}')\langle\mathbf{k}+\mathbf{q}|i\rangle\langle i|\mathbf{k}'+\mathbf{q}'\rangle\end{aligned} \tag{1.12}$$

Here, I introduced the MDFF $S(\mathbf{q},\mathbf{q}')$ and accordingly the real space MDFF (rMDFF) $S(\mathbf{r},\mathbf{r}')$. [1, 12–14] Contrary to the commonly used convention, the $1/q^2{q'}^2$ term was included in the MDFF. Due to the specific properties of the Coulomb interaction $\hat{V}$, the rMDFF can be multiplied with the initial probe wavefunctions whereas the MDFF has to be convolved with them. In order to express the MDFF for a specific system, a basis set for the probe states as well as for the target states has to be chosen. Usually, this is a spherical harmonics basis. For the target's initial state we therefore write $|lm_l\rangle$ and for the final state $|LM_L\rangle$[5]. The lower case letters correspond to the initial states, whereas uppercase letters represent the final states. L and M_L denote the orbital angular momentum quantum number and the magnetic quantum number, respectively. The magnetic quantum number m_l of the initial state is typically unknown, therefore it is necessary to sum

[5]The important parameters for a spherical harmonics basis are l and m_l, therefore the other quantum number such as the principal quantum number n or the spin quantum number s are not written explicitly.

incoherently over m_l. The MDFF then reads [12]

$$\begin{aligned}
S(\boldsymbol{q},\boldsymbol{q}') =& \sum_{F}\sum_{LM_L}\sum_{L'M'_L}\sum_{m_l}\langle F|LM_L\rangle\langle LM_L|\hat{V}(\boldsymbol{q})|lm_l\rangle \\
& \langle lm_l|\hat{V}^{\dagger}(\boldsymbol{q}')|L'M'_L\rangle\langle L'M'_L|F\rangle \\
=& 2\sum_{LM_L}\sum_{L'M'_L}\sum_{\lambda\mu\lambda'\mu'} 4\pi(-1)^{L+L'}i^{\lambda-\lambda'}(2l+1)\sqrt{[\lambda,\lambda',L,L']} \\
& \frac{1}{q^2q'^2}Y^{\mu}_{\lambda}(\tilde{\boldsymbol{q}})^*\langle j_\lambda(q)\rangle_{ElL}Y^{\mu'}_{\lambda'}(\tilde{\boldsymbol{q}}')\langle j_{\lambda'}(q')\rangle_{ElL'} \\
& \begin{pmatrix} l & \lambda & L \\ 0 & 0 & 0 \end{pmatrix}\begin{pmatrix} l & \lambda' & L' \\ 0 & 0 & 0 \end{pmatrix}\sum_{m_l}\begin{pmatrix} l & \lambda & L \\ -m_l & \mu & M_L \end{pmatrix}\begin{pmatrix} l & \lambda' & L' \\ -m_l & \mu' & M'_L \end{pmatrix} \\
& \sum_{\mathbf{k}n} D^{\boldsymbol{k}n}_{LM_L}(D^{\boldsymbol{k}n}_{L'M'_L})^*\delta(E+E_{nlj}-E_{\mathbf{k}n})
\end{aligned} \tag{1.13}$$

with the abbreviation $[l_1,l_2,l_3,...] = (2l_1+1)(2l_2+1)(2l_3+1)\ldots$. λ, λ' and μ, μ' represent the transfer of angular momentum during a transition, e.g. $\lambda = 1$ is a dipole-allowed transition, $\lambda = 2$ is a quadrupole-allowed transition, etc. The different transition types have to fulfill the selection rules $|l-L| \leq \lambda \leq |l+L|$ and $m_l - M_L = \mu$, otherwise they do not contribute. $Y^{\mu}_{\lambda}(\tilde{\boldsymbol{q}})^*$ and $Y^{\mu'}_{\lambda'}(\tilde{\boldsymbol{q}}')$ are the spherical harmonics which depend on the normalized vectors $\tilde{\boldsymbol{q}} = \boldsymbol{q}/q$ as only the direction counts. Further, $\langle j_\lambda(q)\rangle_{ElL}$ is the fully weighted radial wavefunction overlap, where

$$\langle j_\lambda(q)\rangle_{ElL} = \int \mathrm{d}r r^2 u_L(r) j_\lambda(qr) R_l(r) \tag{1.14}$$

is a radial integral involving initial- ($R_l(r)$) and final-state ($u_L(r)$) radial wavefunctions as well as the spherical Bessel function $j_\lambda(qr)$ of order λ. $\left(\begin{smallmatrix} a & b & c \\ d & e & f \end{smallmatrix}\right)$ denotes the Wigner-3j-symbol which is related to the Clebsch-Gordan coefficients. The Wigner-Eckart theorem was used so that the orientation dependence (m_l, M_L, μ) can be separated into the Wigner-3j-symbols and the fully weighted radial wavefunction overlap can be calculated independently. [12] The energy restricted sum over band states in the last line denotes the coupling of different final angular momenta. Eq. 1.13 describes the case of a spin-independent system. Throughout this work, the spin dependency was not taken into account, for the general case, also including the spin-depency, see [15].

The MDFF was introduced above in a rather abstract way. In order to get a more applied picture of it, I will show its connection to the density matrix in a simple example and further show the relation between the double differential scattering cross section and the MDFF. For the relation between the density matrix of the probe electron and the MDFF of the

scatterer, scattering on a single atom will be assumed. This means that only one scattering process takes place. Therefore, neither before nor after the inelastic scattering, elastic scattering processes occur. In general, any state of the incident electron can easily be decomposed into monochromatic plane waves [7], but this is beyond the scope of this work. Then, the density matrix of the probe electron in the diffraction plane after a fixed energy loss E is [16]

$$\rho(\mathbf{q},\mathbf{q}') = \left(\frac{2\pi m e^2}{\varepsilon_0 \hbar^2 k}\right) S\left(\mathbf{q},\mathbf{q}'\right) \tag{1.15}$$

Historically, the MDFF was introduced by Kohl and Rose connecting it with the double differential scattering cross section [13]. For an incident plane wave, the double differential scattering cross section in first order Born approximation reads [14]

$$\frac{\partial^2\sigma}{\partial E \partial \Omega} = \frac{4\gamma^2}{a_0^2}\frac{k'}{k} S(\mathbf{q},\mathbf{q}), \tag{1.16}$$

where $a_0 = 4\pi\varepsilon_0\hbar^2/me^2$ is the Bohr radius, γ is a relativistic factor and $S(\mathbf{q},\mathbf{q})$ is the dynamic form factor (DFF). The DFF is a special case of the MDFF where only the diagonal elements ($\mathbf{q} = \mathbf{q}'$) are considered. Whereas the DFF describes single inelastic scattering of a single incident plane wave as in the example above, the MDFF also takes into account that, the inelastically scattered wave consists of a number of mutually coherent plane waves and in a general case interference terms can occur.

1.3.2 Splitting the MDFF

The MDFF $S(\boldsymbol{q},\boldsymbol{q}')$ (see equation 1.13) can be split into three terms, separating the $\boldsymbol{q}$- and $\boldsymbol{q}'$-dependent terms from the terms not depending on $\boldsymbol{q}$ [15]:

$$\begin{aligned} S(\boldsymbol{q},\boldsymbol{q}') =& \sum_{\alpha,\alpha'} g_\alpha(\boldsymbol{q})^\dagger \Xi_{\alpha,\alpha'} g_{\alpha'}(\boldsymbol{q}') \\ =& \boldsymbol{g}(\boldsymbol{q})^\dagger \cdot \boldsymbol{\Xi} \cdot \boldsymbol{g}(\boldsymbol{q}') \end{aligned} \tag{1.17}$$

with the shorthand notation $\alpha = (\lambda,\mu,L)$ and $\alpha' = (\lambda',\mu',L')$. Equations 1.18 and 1.19 show the terms after regrouping of equation 1.13 according to equation 1.17.

$$g_\alpha(\boldsymbol{q}) = \frac{Y_\lambda^\mu(\tilde{\boldsymbol{q}})\langle j_\lambda(q)\rangle_{ElL}}{q^2} \tag{1.18}$$

$$\begin{aligned}\Xi_{\alpha,\alpha'} =& 2 \sum_{M_L M_L'} 4\pi(-1)^{L+L'}(2l+1)i^{\lambda-\lambda'}\sqrt{[\lambda,\lambda',L,L']} \\ & \begin{pmatrix} l & \lambda & L \\ 0 & 0 & 0 \end{pmatrix} \begin{pmatrix} l & \lambda' & L' \\ 0 & 0 & 0 \end{pmatrix} X_{LM_L L'M_L'} \\ & \sum_{m_l} \begin{pmatrix} l & \lambda & L \\ -m_l & \mu & M_L \end{pmatrix} \begin{pmatrix} l & \lambda' & L' \\ -m_l & \mu' & M_L' \end{pmatrix}\end{aligned} \tag{1.19}$$

$$X_{LM_L L'M_L'} = \sum_{\mathbf{k}n} D^{\boldsymbol{k}n}_{LM_L} (D^{\boldsymbol{k}n}_{L'M_L'})^* \delta(E + E_{nlj} - E_{\mathbf{k}n}) \tag{1.20}$$

As only the matrix $\Xi_{\alpha,\alpha'}$ is dependent on m_l, M_L and M_L', these sums can be performed and the remaining subscripts λ, μ and L are denoted as α. $\boldsymbol{\Xi}$ can be computed in a straight forward way if the XDOS is known (for details see section 2.2). Collecting the terms in such a way as described above, $\boldsymbol{g}$ can be interpreted as a vector of functions and eq. 1.17 can be interpreted as a quadratic form[6]. Now, two identity matrices can be inserted, using the (at this point arbitrary) unitary matrix $\boldsymbol{U}$.

$$S(\boldsymbol{q},\boldsymbol{q}') = \boldsymbol{g}(\boldsymbol{q})^\dagger \cdot \boldsymbol{U}^\dagger \boldsymbol{U} \cdot \boldsymbol{\Xi} \cdot \boldsymbol{U}^\dagger \boldsymbol{U} \cdot \boldsymbol{g}(\boldsymbol{q}') \tag{1.22}$$

Then, we can redefine

$$\tilde{\boldsymbol{g}}(\boldsymbol{q}) = \boldsymbol{U} \cdot \boldsymbol{g}(\boldsymbol{q}) \tag{1.23}$$

$$\tilde{\boldsymbol{\Xi}} = \boldsymbol{U}\boldsymbol{\Xi}\boldsymbol{U}^\dagger \tag{1.24}$$

The matrix U is chosen in such a way that $\tilde{\boldsymbol{\Xi}}$ is a diagonal matrix (see section 2.4 for more details on the matrix diagonalization). This is always possible as the $\boldsymbol{\Xi}$ matrix is hermitian (see also appendix B). After this transformation the MDFF reads

$$\begin{aligned} S(\boldsymbol{q},\boldsymbol{q}') =& \sum_{\alpha,\alpha'} g_\alpha(\boldsymbol{q})^\dagger \Xi_{\alpha,\alpha'} g_{\alpha'}(\boldsymbol{q}') \\ =& \sum_{\alpha,\alpha'} \tilde{g}_\alpha(\boldsymbol{q})^\dagger \tilde{\Xi}_{\alpha,\alpha'} \tilde{g}_{\alpha'}(\boldsymbol{q}') \\ =& \sum_{\alpha} \tilde{g}_\alpha(\boldsymbol{q})^\dagger \tilde{\Xi}_{\alpha,\alpha} \tilde{g}_\alpha(\boldsymbol{q}') \\ =& \sum_{\alpha} \tilde{g}_\alpha(\boldsymbol{q})^\dagger \sqrt{\tilde{\Xi}_{\alpha,\alpha}} \sqrt{\tilde{\Xi}_{\alpha,\alpha}} \tilde{g}_\alpha(\boldsymbol{q}') \\ =& \sum_{\alpha} \bar{g}_\alpha(\boldsymbol{q})^\dagger \bar{g}_\alpha(\boldsymbol{q}') \\ =& \bar{\boldsymbol{g}}(\boldsymbol{q})^\dagger \cdot \bar{\boldsymbol{g}}(\boldsymbol{q}') \end{aligned} \tag{1.25}$$

[6] A quadratic form is defined as a homogeneous polynomial of degree two in a number of variables. [17] For an n-dimensional matrix A with matrix elements a_{ij} the quadratic form is

$$q_A(x_1, x_2, \ldots, x_n) = \sum_{ij} x_i^* a_{ij} x_j. \tag{1.21}$$

using the abbreviation[7] $\bar{\boldsymbol{g}}(\boldsymbol{q}) = \sqrt{\tilde{\boldsymbol{\Xi}}} \cdot \tilde{\boldsymbol{g}}(\boldsymbol{q})$.

This diagonalization procedure drastically reduces the number of terms in the $\boldsymbol{\Xi}$ matrix. As an example, we will consider a WIEN2k calculation with default settings ($0 \leq L, L' \leq 3$) including mono-, di- and quadrupole transitions ($\lambda = 0, 1, 2$). In this case $\boldsymbol{\Xi}$ is a 36×36 matrix consisting of 1296 terms. As $\boldsymbol{\Xi}$ is hermitian, it is sufficient to know the triangular matrix which results in $\frac{36(36+1)}{2} = 666$ terms. Due to selection rules, it is possible that some of the remaining entries vanish as well. However, in general off-diagonal elements remain. These elements indicate correlations between different basis states. Therefore, by performing the diagonalization of the $\boldsymbol{\Xi}$ matrix, we extract this additional information (e.g. symmetries) resulting in uncorrelated basis states and only (at most) 36 non-zero elements remain in the $\boldsymbol{\Xi}$ matrix. The basis set described in section 1.3.1 is the common choice as a starting point and also used by WIEN2k [18]. Using matrix diagonalization, however, it is not only possible to reduce the numerical complexity of the problem but also to find a suitable basis for the system, namely the eigenbasis of the MDFF.

To return from the MDFF to the density matrix, it is easier to use the rMDFF instead of the MDFF, as the MDFF has to be convolved with the initial probe wavefunctions whereas the rMDFF can be multiplied directly with them. The rMDFF is related to the MDFF by Fourier transformation and as the $\boldsymbol{q}$ and $\boldsymbol{q}'$ are decoupled it simply reads

$$\begin{aligned} S(\boldsymbol{r}, \boldsymbol{r}') =& \tilde{\boldsymbol{g}}(\boldsymbol{r})^\dagger \cdot \tilde{\boldsymbol{\Xi}} \cdot \tilde{\boldsymbol{g}}(\boldsymbol{r}') \\ =& \bar{\boldsymbol{g}}(\boldsymbol{r})^\dagger \cdot \bar{\boldsymbol{g}}(\boldsymbol{r}') \end{aligned} \tag{1.26}$$

with the same $\boldsymbol{\Xi}$ matrix as for the MDFF and using the relations

$$\begin{aligned} \tilde{\boldsymbol{g}}(\boldsymbol{r}) &= FT_{\boldsymbol{q}}[\tilde{\boldsymbol{g}}(\boldsymbol{q})] \\ \bar{g}_\alpha(\boldsymbol{r}) &= \sqrt{\Xi_{\alpha\alpha}}\tilde{g}_\alpha(\boldsymbol{r}) \end{aligned} \tag{1.27}$$

Inserting the rMDFF in eq. 1.11 and using $\langle i|\boldsymbol{r}\rangle = \phi(\boldsymbol{r})$ for the wavefunction of the incident probe beam gives the reduced density matrix after a Coulomb interaction

$$\begin{aligned} \boldsymbol{\rho}(\boldsymbol{r}, \boldsymbol{r}') &= \sum_\alpha \bar{g}_\alpha(\boldsymbol{r})^* \bar{g}_\alpha(\boldsymbol{r}') \langle \boldsymbol{r}|i\rangle \langle i|\boldsymbol{r}'\rangle \\ &= \sum_\alpha (\bar{g}_\alpha(\boldsymbol{r})\phi(\boldsymbol{r}))^* \bar{g}_\alpha(\boldsymbol{r}')\phi(\boldsymbol{r}') \end{aligned} \tag{1.28}$$

[7] In this case, the notation of the square root of a matrix can be used, as the matrix $\tilde{\boldsymbol{\Xi}}$ is always diagonal. Then, the square root of each element is taken separatly to form the resulting matrix. In its diagonal form, the elements of the matrix $\tilde{\Xi}_{\alpha,\alpha}$ can be interpreted as the probability p_i that system is found in state $|\psi_i\rangle$, as the MDFF is directly related to the density matrix ($\rho = \sum_i p_i |\psi_i\rangle \langle\psi_i|$). Therefore the diagonal elements are non-negative numbers and the square root can easily be calculated without the use of complex numbes.

In practice, we measure the intensity which for an ideal lens system reads

$$I(\boldsymbol{r}) = \boldsymbol{\rho}(\boldsymbol{r}, \boldsymbol{r}) = \sum_{\alpha} |\bar{g}_{\alpha}(\boldsymbol{r})\phi(\boldsymbol{r})|^2. \tag{1.29}$$

In this theoretical description the fact that before and after the inelastic scattering process the electron wavefunction propagates through the crystal was not included. If we assume that the incoming electron is in a pure state, the elastically scattered electron is still in a pure state until it scatters inelastically. After the inelastic scattering event the diagonalization of the rMDFF then leads to a factorization of the density operator $\hat{\boldsymbol{\rho}} = \sum_{\alpha} p_{\alpha} |\alpha\rangle \langle\alpha|$. The density matrix can then be split into an incoherent sum and the elastic propagator can be applied separately on each coherent term of the sum. As each $|\alpha\rangle$ is in itself in a pure state it can then be propagated through the rest of the crystal elastically using e.g. the multislice approach (for details see section 2.6). [7, 8]

Chapter 2

Implementation

In the following section, it is shown how to get the fully weighted radial wavefunction overlap and why we use it instead of the dipole approximation. Then, I will show how the MDFF including the XDOS is implemented, explaining all necessary transformations, and finally, how it is used for the simulation of the inelastic scattering of fast electrons in a crystal. To calculate and implement the fully weighted radial wavefunction overlap as well as the XDOS, I used the programm package WIEN2k [18] including TELNES.3 [19]. WIEN2k uses a density functional theory (DFT) approach to calculate the electronic structure of solids. The additional package TELNES.3 is used to calculate ELNES spectra in reciprocal space. These improvements were added to the existing multislice program by Martin Zauner. [8]

2.1 The fully weighted radial wavefunction overlap

The fully weighted radial wavefunction overlap (WRWO) $\langle j_\lambda(q)\rangle_{ElL}$ is commonly simplified by the dipole approximation, which replaces $\langle j_\lambda(q)\rangle_{ElL}$ by q up to the cut-off momentum q_c for dipole-allowed transitions (see figure 2.1). Recently, it has been shown that this approximation already breaks down for medium scattering angles and causes significant errors of the order of up to 25% even at small momentum transfer [2]. To get high resolution images, it is necessary to resolve small distances in real space which correspond to big distances in reciprocal space. Hence, an accurate description of $\langle j_\lambda(q)\rangle_{ElL}$ beyond the limitations of the dipole approximation is necessary. Therefore the calculations include the fully weighted radial wavefunction overlap in order to obtain better results.

For the fully weighted radial wavefunction overlap $\langle j_\lambda(q)\rangle_{ElL}$ as defined in equation 1.14 the initial- an the final-state radial wavefunctions are needed, as well as the spherical Bessel function. The intial- and the final-

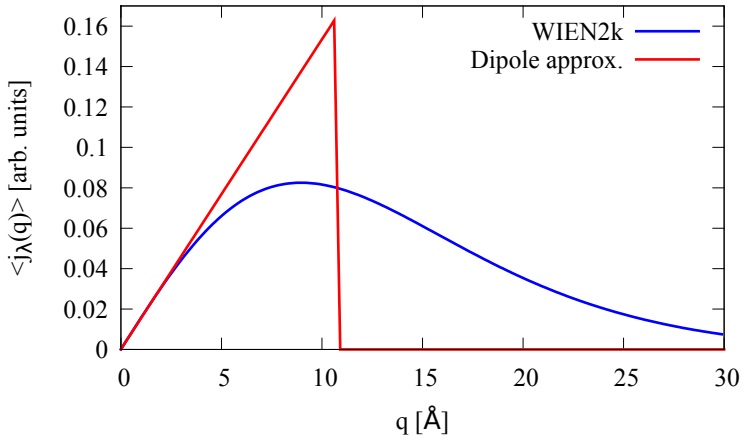

Figure 2.1: The fully weighted radial wavefunction overlap for a dipole-allowed transition from a Ti 2p-state to a final state with d-wave symmetry compared to the dipole approximation for the case of TiO_2. The WRWO was calculated using WIEN2k but atomic models provide a similar result. [20]

state radial wavefunctions are calculated with TELNES.3 using WIEN2k [18, 19]. The steps to calculate the different wavefunctions can be simplified by using the program *extractwf* (written by Stefan Löffler) which calls the different TELNES.3 routines. These wavefunctions are then used by the program *wien2k-wf2fq* (also by Stefan Löffler) and together with the spherical Bessel function the fully weighted radial wavefunction overlap is calculated. It can be specified for which energy and for which transition type $\langle j_\lambda(q)\rangle_{ElL}$ shall be calculated. The outputfile consists of the energy, the set of according quantum numbers and a list of q and $\langle j_\lambda(q)\rangle_{ElL}$ values (see also table 2.1). It can contain the fully weighted radial wavefunction overlap for different sets of parameters. As the fully weighted radial wave-

energy transfer E						
n	$l_{initial}$	j	$n+1$	L	s	λ
q	$\langle j_\lambda(q)\rangle_{ElL}$					
$\vdots$	$\vdots$					

Table 2.1: This table shows how the file containing the fully weighted radial wavefunction overlap is formatted. The unit for the energy transfer E is eV and for the momentum transfer $Å^{-1}$.

function overlap is only given for a range of sampling points, I use spline interpolation to get $\langle j_\lambda(q)\rangle_{ElL}$ for every q-value.

The interpolated fully weighted radial wavefunction overlap is then used together with the spherical harmonics to calculate $g_\alpha(\boldsymbol{q})$ according to equa-

tion 1.18. This calculation is independent of the layer or the atomic site, therefore it can be performed preceeding the computation of the XDOS, which has to be done separately for each position. This approach increases the speed of the simulation compared to earlier implementations where the same WRWO was calculated separately for each atomic site.

2.2 Extracting the XDOS

The cross density of states (XDOS), which is written by TELNES.3 to the file ⟨case⟩.xdos, has a special format and in order to use the XDOS values correctly, I have to change the line-by-line format into a matrix format. TELNES.3 computes the XDOS for different energy values. As a first step, I have to choose the wanted energy and use only the XDOS elements related to that energy. The XDOS connects states with different angular momentum LM and $L'M'$. Instead of having four values (L, M, L' and M') to describe the states, TELNES.3 uses just two values $I = (L+1)^2 - L + M$ and $I' = (L'+1)^2 - L' + M'$ for the different states respectively (see table 2.2). The XDOS in the ⟨case⟩.xdos file is then ordered by $(I \cdot (I-1)/2 + I')$. Further details are documented in the TELNES.3 file *readcrossdos.f*.

L	M	I
0	0	1
1	-1	2
1	0	3
1	1	4
2	-2	5
2	-1	6
⋮	⋮	⋮

Table 2.2: This table shows the corresponding I values for given LM values according to the formula $I = (L+1)^2 - L + M$.

Next to the density operator, which is always hermitian, the XDOS matrix $X_{II'}$ is also a hermitian matrix (see appendix A). Therefore, it is sufficient to know the upper or lower triangular matrix for computing the whole matrix. TELNES.3 manages the data as a lower triangular matrix as shown in table 2.3.

To obtain the full XDOS matrix, I have to fill in the upper triangular matrix with the hermitian conjugate of the lower triangular matrix[1]. After this procedure, I finally have the XDOS matrix in the wanted format and can use it for my further calculations.

[1] One has to avoid counting the diagonal elements twice.

$I \backslash I'$	1	2	3	...
1	1			
2	2	3		
3	4	5	6	
⋮	⋮	⋮	⋮	⋱

Table 2.3: The ordering of the XDOS elements as computed by TELNES.3.

2.3 Matrix rotation

After obtaining the XDOS matrix from WIEN2k and TELNES.3 as described above, I want to diagonalize it and finally use it to calculate the scattering kernels. For these steps different programs are used and therefore one has to take care of the different conventions. In WIEN2k, the calculations for (symmetry-)equivalent atoms at different positions are only done for one site. Therefore, the XDOS matrix has to be translated and rotated properly for each atomic position. The rutile unit cell can be used as an example to illustrate the different rotations (see figure 2.2). The coordinate system at each atomic position indicates how we have to rotate the XDOS matrix in order to get overlapping orbitals. Whereas the titanium atoms (grey balls) at the corners are orientated in the same direction, the titanium atom in the middle is rotated around the z-axis (blue) by 90°. The oxygen atoms (blue balls) are all orientated differently. In figure 2.2 it appears that the oxygen atoms in the upmost layer are orientated in the same direction as the oxygen atoms in the lowest layer, but in fact these layers are identical and just displayed twice to show the unit cell. The next step is a transformation in such a way that the data for each position is described in the same coordinate system, namely in the canonical basis. In case of rutile the data is transformed in the basis system of the unit cell. The final step depends on the angle between the incoming probe electron and the crystal. It rotates the unit cell in the crystallographic direction in which we want to probe it.

All of these transformations are included in the transform matrix for each atomic position. These 3×3 transformation matrices are in a cartesian coordinate system. But the XDOS matrix is given in a spherical harmonics basis and is (with default settings) a 36×36 matrix. To rotate the XDOS matrix properly, these cartesian transformation matrices have to be transformed in such a way that they can be applied to a spherical harmonics basis. In order to do this, the Euler angles and the Wigner $\boldsymbol{D}$-matrices have to be calculated. The Euler angles are used to describe the orientation of a rigid body. Every rotation matrix can be decomposed in a product of three elemental (around a single axis) rotation matrices for the so-called Euler angles (α, β, γ). These angles are then used for the Wigner $\boldsymbol{D}$-matrix which consists of the matrix elements for the rotation operator $\hat{\mathcal{R}}(\alpha, \beta, \gamma)$ in the

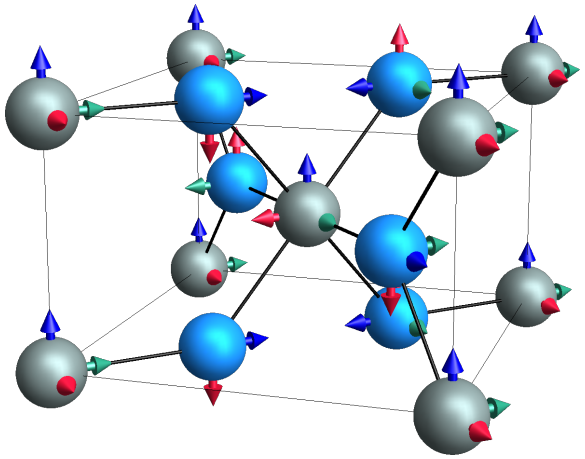

Figure 2.2: The unit cell of rutile (TiO_2) including the internal coordinate system at each atomic position. Grey balls are titanium and blue balls are oxygen. The colors of the arrows indicate the orientation of the (local) coordinate system ([red, green, blue] $\widehat{=}$ [x,y,z]).

$|jm\rangle$ basis to rotate the XDOS matrix in its spherical harmonics basis.

In order to know if a transformation matrix only represents a rotation or also a reflection, we need to calculate the determinant of this matrix. If $\det(\boldsymbol{A}) = +1$, we have a pure rotation matrix, for $\det(\boldsymbol{A}) = -1$, it is a reflection matrix, corresponding to an inversion possibly combined with a rotation. If $|\det(\boldsymbol{A})| \neq 1$, the matrix $\mathbf{A}$ would correspond to a distortion, but this does not occur in our case. In our program, we check if the determinant of the transformation matrix equals -1 and if that is the case, we invert each element of our matrix. As the XDOS is given in a spherical harmonics basis, this inversion gives a factor $(-1)^l$ according to

$$Y_l^m(\pi - \theta, \pi + \phi) = (-1)^l Y_l^m(\theta, \phi). \tag{2.1}$$

The next step is to find out to which rotation angles the resulting matrix corresponds. The Euler-angles (α, β, γ) are a possible representation of the orientation of our atoms (see figure 2.3) and they can be extracted from the rotation matrix. In the Z-Y'-Z" convention, we perform three rotations

$$\begin{pmatrix} \cos\alpha & \sin\alpha & 0 \\ -\sin\alpha & \cos\alpha & 0 \\ 0 & 0 & 1 \end{pmatrix} \cdot \begin{pmatrix} \cos\beta & 0 & -\sin\beta \\ 0 & 1 & 0 \\ \sin\beta & 0 & \cos\beta \end{pmatrix} \cdot \begin{pmatrix} \cos\gamma & \sin\gamma & 0 \\ -\sin\gamma & \cos\gamma & 0 \\ 0 & 0 & 1 \end{pmatrix} \tag{2.2}$$

resulting in a single matrix

$$\begin{pmatrix} c_\alpha c_\beta c_\gamma - s_\alpha s_\gamma & -c_\gamma s_\alpha - c_\alpha c_\beta s_\gamma & c_\alpha s_\beta \\ c_\alpha s_\gamma + c_\beta c_\gamma s_\alpha & c_\alpha c_\gamma - c_\beta s_\alpha s_\gamma & s_\alpha s_\beta \\ -c_\gamma s_\beta & s_\beta s_\gamma & c_\beta \end{pmatrix} \tag{2.3}$$

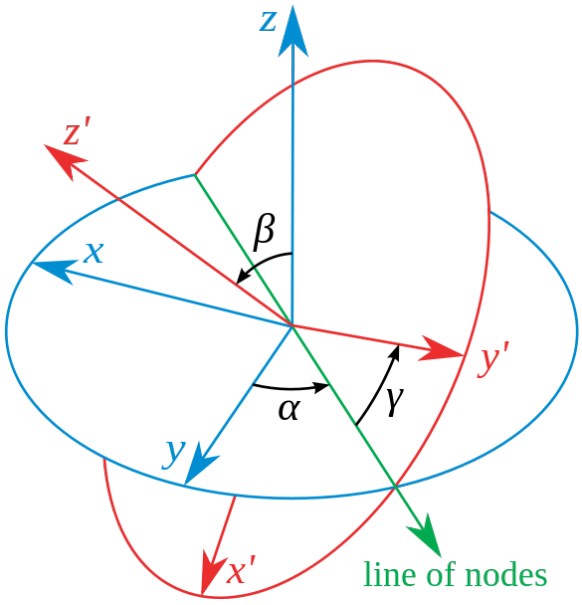

Figure 2.3: Illustration of the Euler angles in the Z-Y'-Z" convention. At first a rotation of α around the z-axis is performed, then a rotation of β around the new y-axis and finally a rotation of γ around the new z-axis. [21]

where c_α is a shorthand notation for $\cos\alpha$ and s_α for $\sin\alpha$.

From comparing this result with the rotation matrix, I can extract the Euler angles. For the Z-Y'-Z" convention, the angles (α, β, γ) for a rotation matrix $\boldsymbol{A}$ read

$$\alpha = \arctan2(A_{13}, A_{23}) \tag{2.4}$$
$$\beta = \arccos(A_{33}) \tag{2.5}$$
$$\gamma = \arctan2(-A_{31}, A_{32}). \tag{2.6}$$

The $\arctan2(y, x)$ function corresponds to the $\arctan(\frac{y}{x})$ but additionally it places the angle in the correct quadrant.

The rotation operator for the Euler angles reads [22]

$$\hat{\mathcal{R}}(\alpha, \beta, \gamma) = e^{-i\alpha\hat{J}_z} e^{-i\beta\hat{J}_y} e^{-i\gamma\hat{J}_z} \tag{2.7}$$

with the total angular momentum operator $\hat{J} = \hat{L} + \hat{S}$. In the $|jm\rangle$-basis, the rotation operator is the Wigner $\boldsymbol{D}$-matrix, which is a square matrix of dimension $2j + 1$ [22]

$$D^j_{m'm}(\alpha, \beta, \gamma) \equiv \langle jm'|\hat{\mathcal{R}}(\alpha, \beta, \gamma)|jm\rangle = e^{-im'\alpha} d^j_{m'm}(\beta) e^{-im\gamma} \tag{2.8}$$

with Wigner's (small) $\boldsymbol{d}$-matrix

$$d^j_{m'm}(\beta) = \langle jm'|e^{-i\beta\hat{J}_y}|jm\rangle. \tag{2.9}$$

Evaluating equation 2.9, the small $\boldsymbol{d}$-matrix reads [22]

$$\begin{aligned} d^j_{m'm}(\beta) = &[(j+m')!(j-m')!(j+m)!(j-m)!]^{1/2} \\ &\times \sum_s \frac{(-1)^{m'-m+s}}{(j+m-s)!s!(m'-m+s)!(j-m'-s)!} \\ &\times \left(\cos\frac{\beta}{2}\right)^{2j+m-m'-2s} \left(\sin\frac{\beta}{2}\right)^{m'-m+2s} \end{aligned} \tag{2.10}$$

where the sum over s is over such values that the factorials are nonnegative. Further, the relation for swapped mm'-values reads [22]

$$d^j_{m',m} = (-1)^{m-m'} d^j_{m,m'} = d^j_{-m,-m'}. \tag{2.11}$$

With this formalism an adequate rotation of the XDOS in a spherical harmonics basis is possible.

2.4 Matrix diagonalization

A square matrix $\boldsymbol{A}$ is diagonalizable if it is similar to a diagonal matrix, that means that there exists an invertible matrix $\boldsymbol{U}$ such that $\boldsymbol{U}^{-1}\boldsymbol{A}\boldsymbol{U}$ is a diagonal matrix. The diagonal entries of the diagonalized matrix $\boldsymbol{A}$ are the eigenvalues of $\boldsymbol{A}$.

$$\boldsymbol{U}^{-1}\boldsymbol{A}\boldsymbol{U} = \begin{pmatrix} \lambda_1 & 0 & 0 & \\ 0 & \lambda_2 & 0 & \dots \\ 0 & 0 & \lambda_3 & \\ & \vdots & & \ddots \end{pmatrix} = \mathrm{diag}(\lambda_i) \tag{2.12}$$

Converting this equation lets us identify it as a system of eigenvalue equations.

$$\boldsymbol{A}\boldsymbol{U} = \boldsymbol{U} \begin{pmatrix} \lambda_1 & 0 & 0 & \\ 0 & \lambda_2 & 0 & \dots \\ 0 & 0 & \lambda_3 & \\ & \vdots & & \ddots \end{pmatrix} \tag{2.13}$$

Then, it follows that the matrix $\boldsymbol{U}$ consists of the eigenvectors as column vectors. If the matrix $\boldsymbol{A}$ is hermitian, then the eigenvectors of $\boldsymbol{A}$ can be chosen to form an orthonormal basis. In this case, the matrix $\boldsymbol{U}$ is a unitary matrix.

Due to selection rules, the matrix I want to diagonalize can include rows and columns consisting just of zeros. So it can be (and in most situations will be) singular, which means that it has no inverse. The LAPACK routine to find the eigenvalues and eigenvectors of a matrix could not handle this case properly. Therefore, a different computational approach has to be used: the Schur decomposition.

The Schur decomposition reads as follows: if $\boldsymbol{A}$ is an $n \times n$ square matrix with complex entries, then $\boldsymbol{A}$ can be expressed as

$$\boldsymbol{A} = \boldsymbol{U}^{-1}\boldsymbol{B}\boldsymbol{U} \tag{2.14}$$

where $\boldsymbol{U}$ is a unitary matrix (so that its inverse $\boldsymbol{U}^{-1}$ is also the conjugate transpose $\boldsymbol{U}^{\dagger}$ of $\boldsymbol{U}$), and $\boldsymbol{B}$ is an upper triangular matrix, which is called a Schur form of $\boldsymbol{A}$. Since $\boldsymbol{B}$ is similar to $\boldsymbol{A}$, it has the same multiset of eigenvalues, and since it is triangular, those eigenvalues are the diagonal entries of $\boldsymbol{B}$. If $\boldsymbol{A}$ is a normal matrix ($\boldsymbol{A}^*\boldsymbol{A} = \boldsymbol{A}\boldsymbol{A}^*$), the Schur form is a diagonal matrix and the column vectors of the matrix $\boldsymbol{U}$ are the eigenvectors [23]. Then, the Schur decomposition is called a spectral decomposition. If the matrix $\boldsymbol{B}$ is positive definite, that means if $\boldsymbol{z}^{\dagger}\boldsymbol{B}\boldsymbol{z}$ is real and positive for all non-zero complex vectors $\boldsymbol{z}$, the Schur decomposition of $\boldsymbol{A}$ and its singular value decomposition coincide.

In this work, I applied the matrix diagonalization to the MDFF $S(\boldsymbol{q}, \boldsymbol{q}')$ in order to transform it to a more suitable basis. According to equation 1.24, the matrix $\boldsymbol{\Xi}$ has to be diagonalized. As the $\boldsymbol{\Xi}$ matrix is hermitian (see appendix B), it follows that it can be diagonalized by a unitary matrix. The eigenvalues for a hermitian matrix are always real, therefore the diagonal matrix $\tilde{\boldsymbol{\Xi}}$ consist of real entries only. The Schur decomposition is performed by a LAPACK routine. It returns the diagonal matrix as well as the transformation matrix.

2.5 Shift theorem

So far, the calculation and diagonalization of the MDFF was discussed rather theoretically. But during the implementation of the MDFF also practical problems occur. After the calculation of the scattering kernels, they need to be shifted onto their respective atomic positions. In the crystal periodic boundary conditions were assumed. Computationally, this position shift was implemented originally using the modulo operator. But using the modulo operator, which gives the remainder of a division, leads to a serious problem as its result is always an integer. This can cause serious problems as the scattering kernel cannot be shifted by a fractional (subpixel) value and it can therefore be placed on the atomic position only within the pixel resolution of the image. If the atomic position and the position of the scattering kernel do not coincide, then the image is not symmetric. In order to get subpixel resolution, a different approach has to be used. According to the shift theorem, translations in real space can be replaced with multiplications in reciprocal space. That means a shift in the spatial position corresponds to a linear phase term in the momentum space.

$$FT\{f(x - x_0, y - y_0)\} = e^{-i(k_x x_0 + k_y y_0)} F(k_x, k_y) \tag{2.15}$$

The first step, in order to use the shift theorem, is to Fourier transform the scattering kernel. Then, to perform the spatial translation, it is multiplied with the linear phase term and finally we use a Fourier back transform to get the scattering kernel again in real space. These steps have to be performed for each layer and each atomic position. By using this procedure instead of the modulo operator, the scattering kernel is placed correctly at the atomic position with sub-pixel accuracy.

2.6 Elastic scattering

So far only inelastic scattering was discussed in this thesis, but as the density matrix has to be propagated elastically through the crystal before and after the inelastic scattering event happens, we will focus on the elastic scattering process in this section. Assuming that the incoming electron is in a pure state, it is still in a pure state after the elastic scattering event. Therefore we use the wavefunction description instead of the formally equivalent density matrix formalism. As elastic scattering is not the central topic of this thesis, this section follows closely the elaborations in references 7 and 8.

The time-independent Schrödinger equation with the electrostatic potential $V(x, y, z)$ of the specimen is used as a starting point for the description of the full electron wavefunction $\psi_f(x, y, z)$.

$$\left(-\frac{\hbar^2}{2m}\nabla^2 - eV(x, y, z)\right)\psi_f(x, y, z) = E\psi_f(x, y, z) \tag{2.16}$$

Typical acceleration voltages of the order of 60 to 300 kV require a relativistic treatment of the electron, namely with the Dirac equation. In a simpler apprach, we take the non-relativistic Schrödinger equation but use the relativistic mass $m = \gamma m_0$. The full wavefunction $\psi_f(x, y, z)$ can be separated into a factor describing a plane wave travelling at a large velocity in the z direction and a factor describing small perturbation effects due to the specimen.

$$\psi_f(x, y, z) = \psi(x, y, z)\exp\left(\frac{2\pi i z}{\lambda}\right) \tag{2.17}$$

where λ is the electron wavelength which is related to the wave vector k by the relation $\lambda = \frac{1}{k}$. Then the kinetic energy of the electron reads

$$E = \frac{\hbar^2 k^2}{2m} = \frac{\hbar^2}{2m\lambda^2}. \tag{2.18}$$

According to the separation of the full wavefunction, we also split the Laplacian $\Delta = \nabla^2$ into a sum of second derivatives which act only on the separate coordinates.

$$\nabla^2 = \frac{\partial^2}{\partial \vec{r}^2} = \frac{\partial^2}{\partial x^2} + \frac{\partial^2}{\partial y^2} + \frac{\partial^2}{\partial z^2} \tag{2.19}$$

After applying the separated ∇^2-operator on the splitted wavefunction, equation 2.16 reads

$$-\frac{\hbar^2}{2m}\left(\nabla_{xy}^2+\frac{\partial^2}{\partial z^2}+\frac{4\pi i}{\lambda}\frac{\partial}{\partial z}+\frac{2meV(x,y,z)}{\hbar^2}\right)\psi(x,y,z)=0. \tag{2.20}$$

As a next step, we use the paraxial approximation which is sometimes referrred to as ignoring the backscattered electrons. That means ψ is only slowly changing with respect to z. Additionally, as λ is small, the second derivative in z can be neglected.

$$\left|\frac{\partial^2}{\partial z^2}\psi\right| << \left|\frac{1}{\lambda}\frac{\partial}{\partial z}\psi\right| \tag{2.21}$$

Then the Schrödinger equation can be simplified to

$$\begin{aligned}\frac{\partial}{\partial z}\psi(x,y,z)&=\left(\frac{i\lambda}{4\pi}\nabla_{xy}^2+i\frac{2me\lambda}{4\pi\hbar^2}V(x,y,z)\right)\psi(x,y,z)\\&=\left(\frac{i\lambda}{4\pi}\nabla_{xy}^2+i\sigma V(x,y,z)\right)\psi(x,y,z)\end{aligned} \tag{2.22}$$

with the interaction parameter $\sigma=\frac{2me\lambda}{4\pi\hbar^2}$. This result can be used to describe the elastic propagation of the wavefunction $\psi(x,y,z)$ from a depth z to $z+\delta z$. Integration from z to $z+\delta z$ where δz is a small slice of the specimen yields

$$\psi(x,y,z+\delta z)=\exp\left(\int_z^{z+\delta z}\left(\frac{i\lambda}{4\pi}\nabla_{xy}^2+i\sigma V(x,y,z)\right)\mathrm{d}z\right)\psi(x,y,z). \tag{2.23}$$

After performing the integration $\psi(x,y,z+\delta z)$ can be simplified to

$$\psi(x,y,z+\delta z)=\exp\left(\delta z\frac{i\lambda}{4\pi}\nabla_{xy}^2+i\sigma V_z(x,y)\right)\psi(x,y,z) \tag{2.24}$$

using the abbreviation

$$V_z(x,y)=\int_z^{z+\delta z}V(x,y,z)\mathrm{d}z. \tag{2.25}$$

After further approximation the wavefunction can be expressed as

$$\begin{aligned}\psi(x,y,z+\delta z)&=\exp\left(\delta z\frac{i\lambda}{4\pi}\nabla_{xy}^2\right)\exp\left(i\sigma V_z(x,y)\right)\psi(x,y,z)\\&=\exp\left(\delta z\frac{i\lambda}{4\pi}\nabla_{xy}^2\right)t(x,y,z)\psi(x,y,z)\end{aligned} \tag{2.26}$$

with the transmission function $t(x,y,z)=\exp\left(i\sigma V_z(x,y)\right)$. As a next step the Fourier transform of the wavefunction $\psi(x,y,z+\delta z)$ can be calculated.

$$\begin{aligned}\mathrm{FT}[\psi(x,y,z+\delta z)]&=\mathrm{FT}\left[\exp\left(\delta z\frac{i\lambda}{4\pi}\nabla_{xy}^2\right)t(x,y,z)\psi(x,y,z)\right]\\&=\exp\left(-i\pi\delta z\lambda(k_x^2+k_y^2)\right)\mathrm{FT}[t(x,y,z)\psi(x,y,z)]\\&=\mathrm{FT}[p(x,y,\delta z)]\mathrm{FT}[t(x,y,z)\psi(x,y,z)]\end{aligned} \tag{2.27}$$

Here $p(x, y, \delta z) = \frac{1}{i\lambda\delta z} \exp(\frac{i\pi}{\lambda\delta z}(x^2 + y^2))$ is the propagation function. A multiplication in reciprocal space corresponds to a convolution in real space. Therefore the propagation from a depth z to $z + \delta z$ can be expressed by a convolution of the two functions $p(x, y, z)$ and $t(x, y, z)$ together with the wavefunction $\psi(x, y, z)$. Then the wavefunction $\psi(x, y, z + \delta z)$ at a depth $z + \delta z$ reads

$$\psi(x, y, z + \delta z) = p(x, y, \delta z) * [t(x, y, z)\psi(x, y, z)] + \mathcal{O}(\delta z^2) \tag{2.28}$$

This result is the basis of the multislice approach. Within this approach the specimen is split into thin slices in the x, y-plane and at each slice the electron wavefunction experiences a phase shift due to the projected atomic potential of all atoms in the slice. If the slices in the specimen are labeled $n = 0, 1, 2, ...$ then equation 2.28 can be written as

$$\psi_{n+1}(x, y) = p_n(x, y, \delta z) * [t_n(x, y)\psi_n(x, y)] + \mathcal{O}(\delta z^2). \tag{2.29}$$

Every slice is treated as a transmission step which is followed by the propagation through vacuum to the next slice. In order to perform the elastic propagation of the incoming wavefunction through the crystal numerically, we use the operator $\hat{T}_j$ to describe the elastic scattering at slice j and the propagation to the next slice.

$$\hat{T}_j = \mathcal{F}^{-1}\hat{p}_j\mathcal{F}\hat{t}_j \tag{2.30}$$

Here $\mathcal{F}$ denotes the Fourier transform, $\hat{p}_j$ and $\hat{t}_j$ are the propagation and the transmission operator for slice j, respectively. For an incoming wavefunction $\psi_0(x, y)$, the wavefunction at a depth d which consists of n slices can be expressed as a consecutive application of the operator $\hat{T}_j$.

$$\psi_n(x, y) = \hat{T}_n\hat{T}_{n-1} \dots \hat{T}_2\hat{T}_1\hat{T}_0\psi_0(x, y) \tag{2.31}$$

Chapter 3

Simulations

The selection of a proper sample material is of utmost importance in order to map atomic orbitals. If the investigated system is too symmetric e.g., it has a cubic unit cell, then all components of an orbital completely overlap resulting in spheres as their individual shapes overlap. This effect can be explained with the partial density of states (pDOS). For a system with lower symmetry the pDOS for an orbital can split up into different partial ratios. E.g. for a p-shaped orbital the pDOS can split up into differently distributed p_x-, p_y- and p_z-shaped orbitals (see figure 3.10).

I have chosen two example materials: lime (CaO) and rutile (TiO_2). Lime is a symmetric material with a cubic unit cell whereas rutile is has a lower symmetry and has a distorted unit cell.

3.1 Lime CaO

The unit cell of lime (see figure 3.1) is cubic causing no splitting of p-orbitals in the pDOS. For the parameter set used in the WIEN2k calculation see appendix C. The central oxygen atom inherits an octrahedral symmetry as the six calcium atoms form an octahedron around it which results in an energy splitting of the d-orbitals (see figure 3.2). The d_{xy}-, d_{xz}- and d_{yz}-orbitals of the oxygen atom are farther away from the calcium atoms than the d_{z^2}- and $d_{x^2-y^2}$-orbitals. Therefore the bound states of the d_{z^2}- and $d_{x^2-y^2}$-orbitals are lower in energy than the d_{xy}-, d_{xz}- and d_{yz}-orbitals. This then translates to the fact that the antibonding states d_{xy}, d_{xz} and d_{yz}, which are referred to as t_{2g}, have a lower energy than the antibonding d_{z^2} and $d_{x^2-y^2}$ which are called e_g. For a material whose pDOS does not show orbital splitting, each block of the XDOS matrix $\mathbf{\Xi}$ which corresponds to a different transition type, e.g., monopole, dipole, etc. is proportional to the identity matrix with a different prefactor. The orbital splitting of the d-orbitals in lime may change the elements in the XDOS matrix $\mathbf{\Xi}$ in such a way that the quadrupole-block in $\mathbf{\Xi}$ is not proportional to the identity

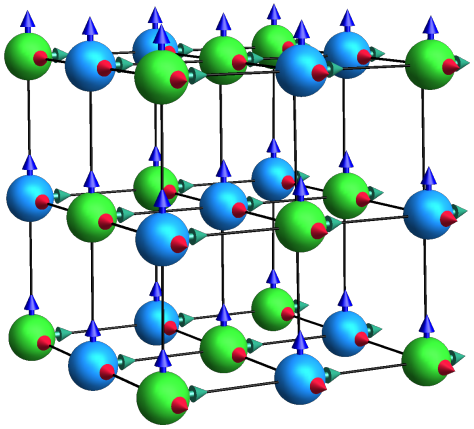

Figure 3.1: The unit cell of lime (CaO). The green balls represent the calcium atoms and the blue balls represent the oxygen atoms. The arrows represent the local coordinate systems. For details see section 2.3.

matrix anymore.

EFTEM-Simulations at 200 keV incident beam energy for the oxygen K-edge in lime were performed for an energy loss of 7 eV (indicated in the DOS, see figure 3.2) above the edge onset in the [0 0 1] zone axis. To elucidate the underlying physics, we simulated a thin sample (one unit cell thick) and assumed ideal lenses. The calculated EFTEM image for a dipole allowed transition is shown in figure 3.3. The blue boxes in each figure show the unit cell in the particular direction. Blue balls indicate oxygen atoms and green balls calcium atoms, as already seen in figure 3.1. Figure 3.3 shows a circular symmetry resulting from the incoherent summation of the p_x-, p_y- and p_z-orbitals. The actual spherical symmetry appears as a circular symmetry in the planar projection. Some of the resulting rings appear larger than others. This behaviour originates from the fact that these rings stem from oxygen atoms which are in a different layer than the others. After the scattering event, the resulting wavefunction propagates through the rest of the crystal. The probe electron wavefunction is highly localized directly after the scattering event at the atomic positions. Due to the Heisenberg uncertainty principle, a high localization in real space leads to a large spread in momentum space. The wavefunction is therefore divergent and it gets larger with increasing propagation distance. Depending on the position of the layer in the crystal, the travelled distance varies and with it the spread of the wavefunction.

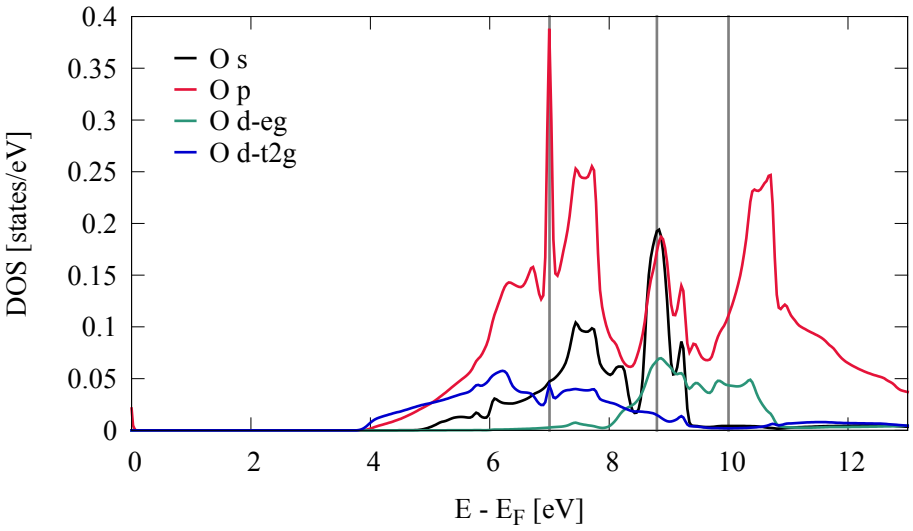

Figure 3.2: The partial DOS (pDOS) of lime including the splitting of the d-orbital into e_g and t_{2g} due to crystal field effects. The energy losses for the performed simulations are indicated at 7, 8.8 and 10 eV.

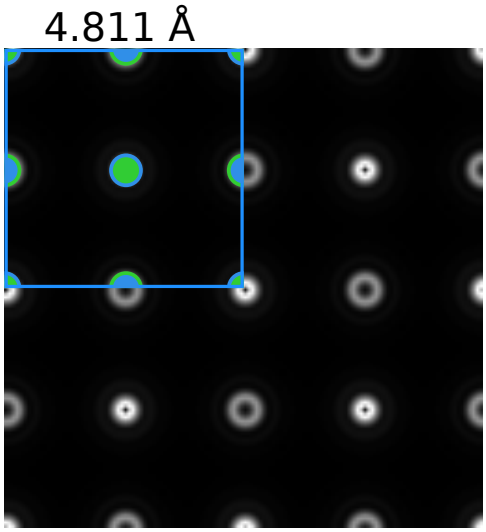

Figure 3.3: Simulation of lime in the [0 0 1] zone axis with a sample thickness of one unit cell (4.811 Å) for an energy loss of 7 eV above the edge onset for dipole-allowed transitions. 200 keV incident beam energy and ideal lenses were assumed.

3.1.1 Thickness dependence

As it is nearly impossible in actual experiments to prepare samples which are only one unit cell thick, we also performed simulations for samples with more realistic thicknesses. Figure 3.4 shows four EFTEM images with the same parameters as in figure 3.3 but for four different thicknesses: 0.4811 nm (one unit cell), 5, 10 and 20 nm. For a thicker sample the number of scattering centers increases and scattering processes in each layer contribute to the final image. The thicker the sample, the more the wavefunction for scattering centers at the beginning of the sample is spread out. Intensities off the atomic sites are the result of these spreaded wavefunctions and their (incoherent) overlap with wavefunctions of different scattering centers. Further, if the sample gets thicker channeling effects become relevant. [5] As the electron wave expands it reaches the potential of the other calcium and oxygen atoms after a certain distance. In this strong potential electrons channel through the sample and we get a high intensity at the sites of the oxygen atoms. Instead of interacting with separate atoms, the electrons interact with nuclear planes or chains. In this case we cannot see a ring shape any more but we get a blurred circular shape.

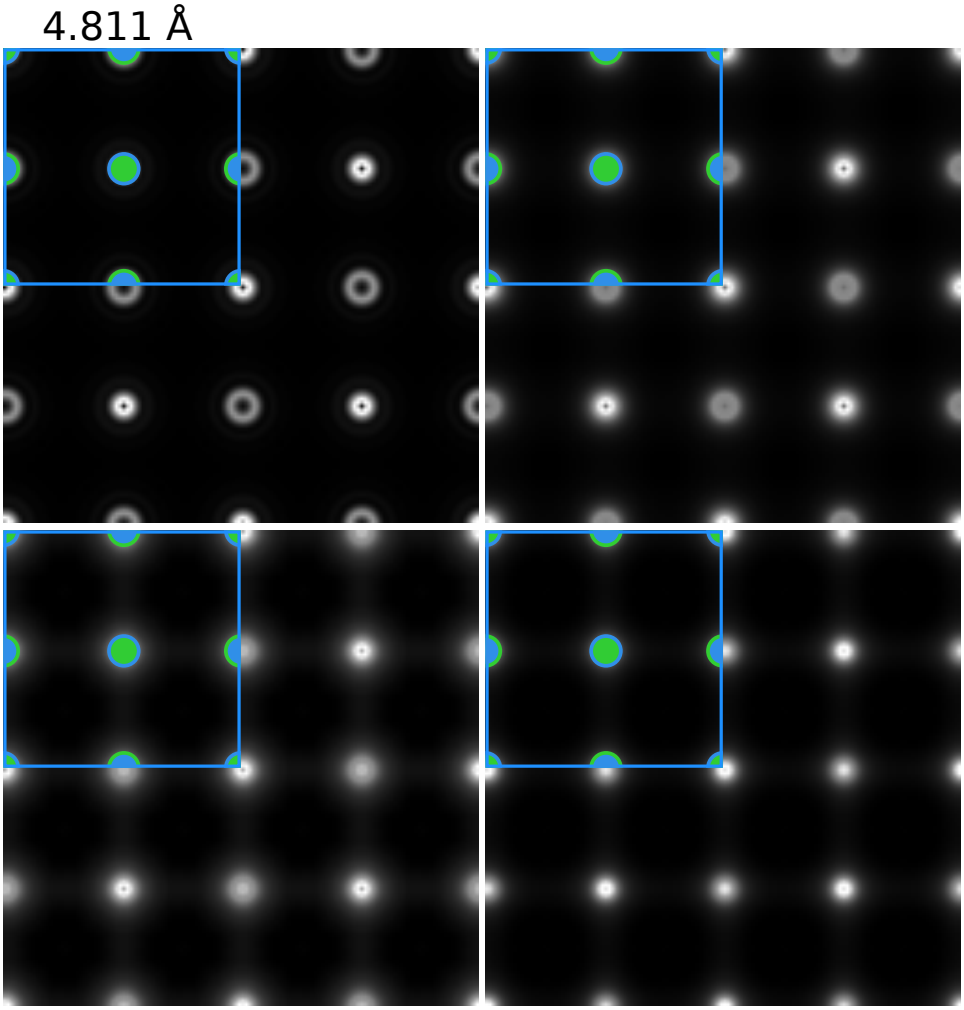

Figure 3.4: Simulation of lime in the [0 0 1] zone axis with different sample thicknesses of 0.4811 nm (one unit cell), 5, 10 and 20 nm (left to right, top to bottom) for an energy loss of 7 eV above the edge onset for dipole-allowed transitions. 200 keV incident beam energy and ideal lenses were assumed.

3.1.2 Aberrations

So far we assumed a set of ideal lenses, but in order to get predictions for actual experiments, we also performed simulations with realistic values for the lens-system. Figure 3.5 shows a comparison of the three different sets of lens parameters given in table 3.1 for the same transition parameters as in figure 3.3. These lens parameter sets refer to the imaging lenses and not to the probe forming lenses. For a parameter set of the FEI Tecnai G^2 F20 or of the FEI Titan G^2 60-300 (which has a C_S corrected lens system) comparisons with experiments are possible.

	Ideal	FEI Tecnai	FEI Titan
Spherical aberration C_S [mm]	0.0	1.2	0.0
Defocus [Å]	0.0	658	0.0
Objective aperture [mrad]	90	18	31

Table 3.1: This table shows the parameter sets of the lens-system for three different TEM types.

For a first comparison of the different parameter sets a sample thickness of 4.811 Å (one unit cell) was chosen. From figure 3.5 it can be seen that while with a Titan microscope the orbital ring shape is spread and blurred but still visible, with a Tecnai microscope this is not the case. Whereas for a set of ideal lenses and for lenses like in a Titan microscope the highest intensities in the EFTEM image are at the atomic sites, this is exactly the opposite for a set of lenses as in a Tecnai microscope. This effect can be explained with the transfer function $T(\boldsymbol{u})$ which depends on the apertures, the attenuation of the wavefunction and the aberration of the lens system. [5] Here $\boldsymbol{u}$ is a vector in reciprocal space. A negative transfer function $T(\boldsymbol{u})$ results in a positive phase contrast and the atoms appear dark. For a positive $T(\boldsymbol{u})$ the phase contrast is negative and the atoms appear bright. Beside of that intensity inversion the orbitals for the different oxygen atoms in a Tecnai microscope do not show a ring shape anymore but rather resemble a filled circle.

In realisic samples for actual experiments both effects, the sample thickness as well as the lens aberrations, play together. To be able to compare simulations and experiments both effects have to be taken into account. Figure 3.6 shows nine EFTEM images with a variation of the sample thickness (top to bottom) versus the three different parameter sets for the lens system (left to right). While the thickness dependence for a set of ideal lenses, which was already discussed in section 3.1.1, does not change the general appearance of the image, it does for the other parameter sets for the lens system. For a lens system like in a Tecnai microscope, the orbitals in a sample 5 nm thick show a roughly circular shape but are wider spread and more blurred than for a one unit cell thick sample as shown in figure 3.5.

For a sample thickness of 10 nm no atomic positions or orbital shapes can be made out. For an even thicker sample of 20 nm the shape of the image changes but the atomic structure of the material is again visible possibly because of channeling effects. But one has to be careful as no information about the structure of the orbitals can be deduced from this. Although for these parameters the orbital shape shows fourfold symmetry we are observing *p*- and not *d*-orbitals. The images in the right column for a set of lens parameters as in a Titan microscope clearly resemble the images for an ideal lens system (left column) but the orbitals are more extended and blurred. The spread of the wavefunction can be seen as a ring around the atomic position which broadens with the sample thickness. For a thin sample this ring is located close around the atomic position. For a sample thickness of 10 nm the rings of neighbouring atoms overlap in the middle between them. But in contrast to a Tecnai microscope the atomic positions as well as the orbital shape can be made out with a Titan microscope. For an even thicker sample (20 nm) channeling effects occur and the highest intensity is at the position of the oxygen atoms.

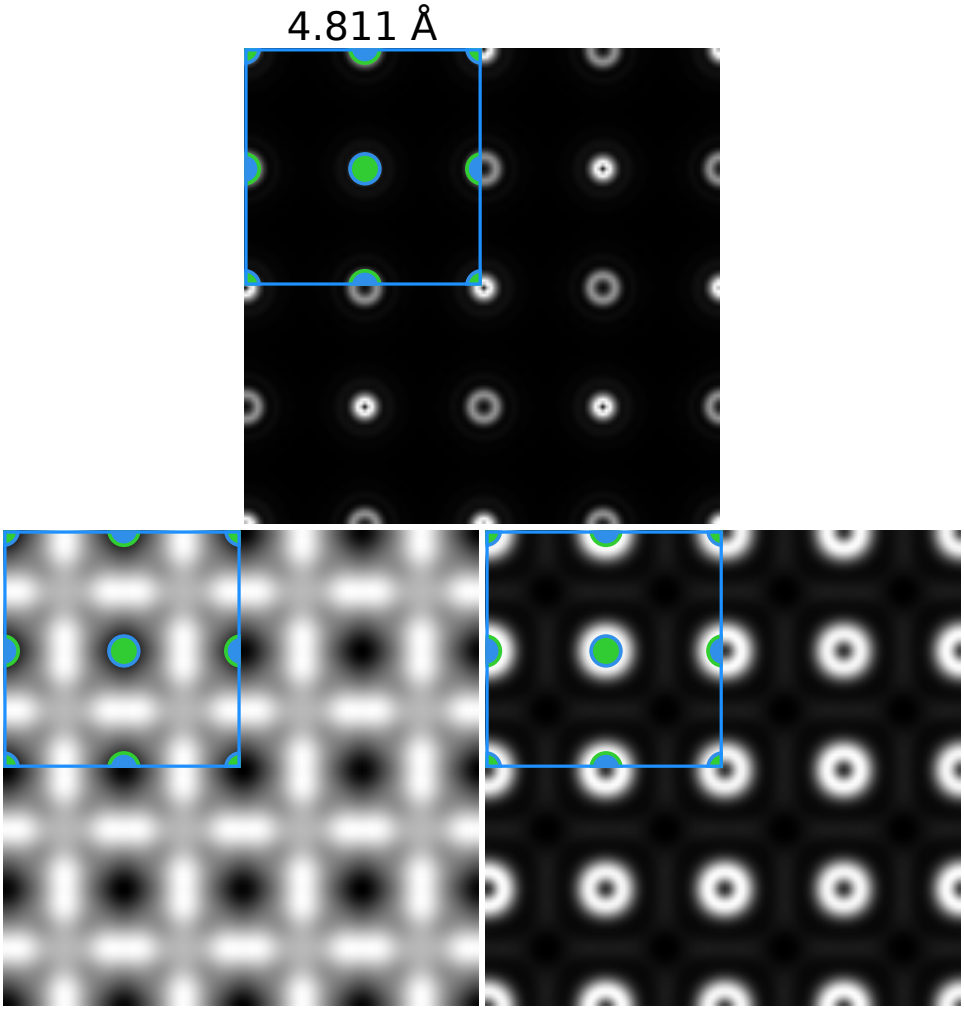

Figure 3.5: Simulation of lime in the [0 0 1] zone axis with a sample thickness of one unit cell (4.811 Å) for an energy loss of 7 eV above the edge onset for dipole-allowed transitions. 200 keV incident beam energy and three different parameters sets for the lens system (see table 3.1) were assumed: Ideal lenses (top), lenses as in a Tecnai microscope (bottom, left) and lenses as in a Titan microscope (bottom, right).

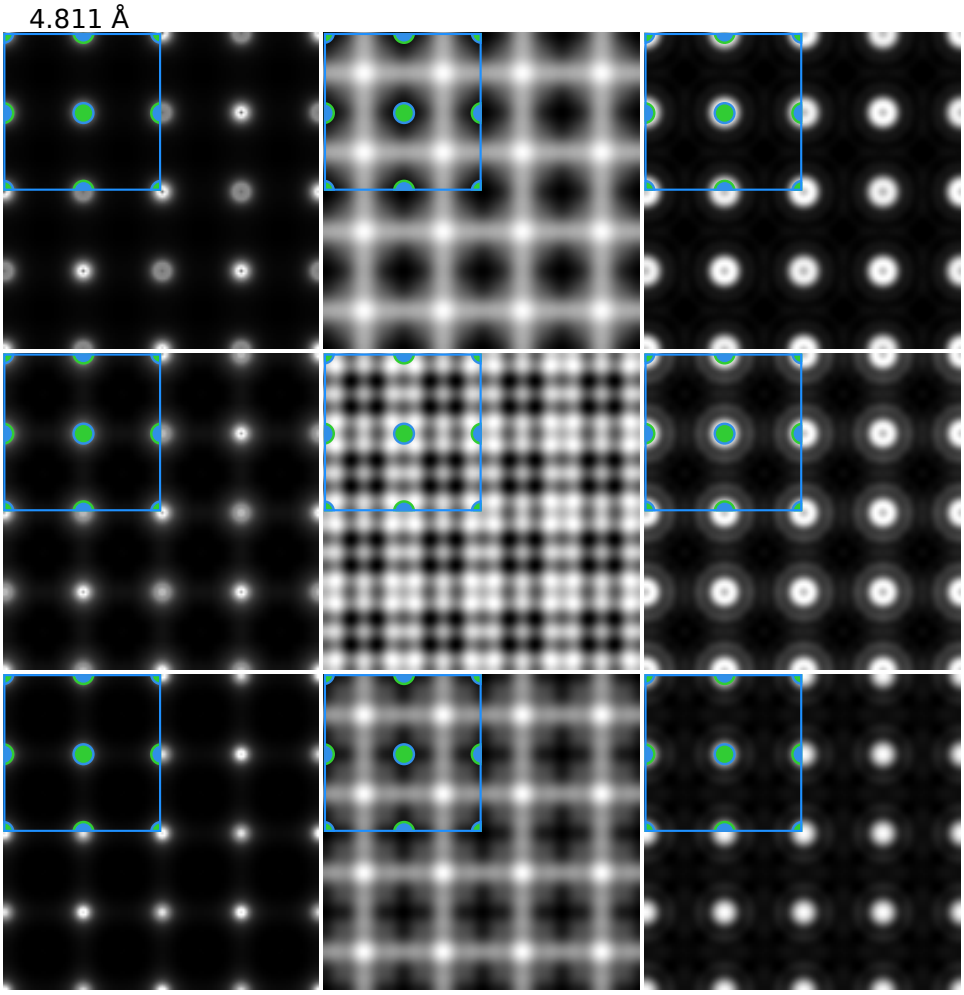

Figure 3.6: Simulation of lime in the [0 0 1] zone axis with different sample thicknesses of 5, 10 and 20 nm (top to bottom) for an energy loss of 7 eV above the edge onset for dipole-allowed transitions. 200 keV incident beam energy and three different parameters sets for the lens system (see table 3.1) were assumed: Ideal lenses (left column), lenses as in a Tecnai microscope (middle column) and lenses as in a Titan microscope (right column).

3.1.3 Beyond dipole

So far no orbital shape, i.e. a dumbbell shape for p-orbitals, was observed due to the degeneracy of the different p-orbitals. But from the pDOS in figure 3.2 it can be seen that degeneracy of the d-orbitals is lifted which can be explained by the octahedral symmetry around the central oxygen atom. We performed EFTEM simulations for quadrupole allowed transitions for two different energies in order to see the splitting of the two different d-orbitals, e_g and t_{2g}. At 7 eV energy loss above the edge onset only the t_{2g} orbitals contribute whereas at 10 eV energy loss only the e_g orbitals contribute. The EFTEM simulations for these energies (see figure 3.7) clearly show a four-fold symmetry in both cases. Further it can be seen that the t_{2g}-orbitals are pointing in the direction of the other oxygen atoms whereas the e_g-orbitals rotated by 90° and are orientated in direction of the calcium atoms. The effects of quadrupole-allowed transitions are very weak, in case of lime the intensity of the quadrupole transition is only 0.02% of the intensity of the dipole transition.

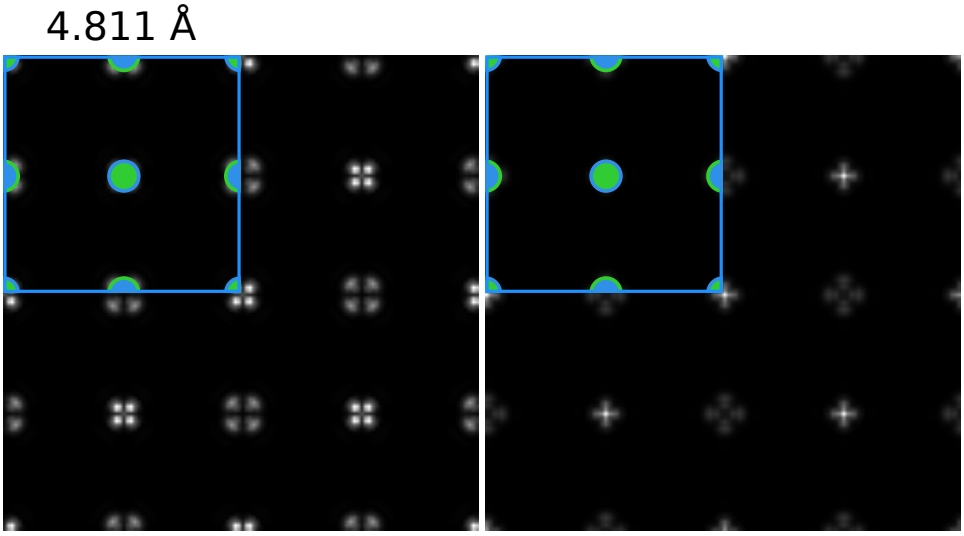

Figure 3.7: Simulation of lime in the [0 0 1] zone axis with a sample thickness of one unit cell (4.811 Å) for an energy loss of 7 (left) and 10 eV (right) above the edge onset for quadrupole-allowed transitions. 200 keV incident beam energy and ideal lenses were assumed.

3.1.4 Multipole coupling

Instead of looking at dipole-allowed and quadrupole-allowed transitions alone, we also performed calculations taking into account the coupling between monopole transitions, dipole transitions and quadrupole transitions. For most energy losses the coupling term can have an important impact on the resulting EFTEM-images, but for some specific energy losses it does not occur. So in order to get a coupling term, it is necessary to choose the energy loss properly. That means that two or more different orbitals, e.g. an s-orbital as well as p-orbitals or even more orbitals occur in the pDOS at that particular energy loss. At 8.8 eV above the edge onset in lime are the s-, p-, e_g and t_{2g}-orbitals overlapping as seen in figure 3.2. Figure 3.8 shows a comparison of the EFTEM images for monopole, dipole and quadrupole transitions as well as an image in which all of these transition types were taken into account at the same time. For a monopole transition a circular symmetry is seen. This is expected as the s-orbital has spherical symmetry. For the dipole transition again a circular symmetry is seen, due to the degeneracy of the p-orbitals. At 8.8. eV energy loss above the edge onset mostly e_g-orbitals contribute for a quadrupole-allowed transition whereas the t_{2g}-oribtals are less pronounced. The shape of the orbitals for a quadrupole-allowed transition therefore resembles the shape of the e_g-orbitals as seen in figure 3.7. Calculations including monopole, dipole and quadrupole transitions at the same time look similar to the dipole transition. This stems from the fact that dipole-allowed transition has by far the most impact on the resulting image. The intensity of the image where all three transition types play together accounts for 101.2% if we scale the term for dipole transition to 100%, whereas the monopole (16%) and especially the quadrupole (0.02%) transition play a minor role.[1] By subtracting the monopole, the dipole and the quadrupole transition image from the total image, where all these effects play together, we get an idea about the coupling between them.

$$I_{coupling} = I_{\lambda=0,1,2} - I_{\lambda=0} - I_{\lambda=1} - I_{\lambda=2} \tag{3.1}$$

For this system the coupling term plays nearly no role as it accounts only for 0.0001% of the intensity in the image for a dipole-allowed transition. With the improved simulation program it is possible to simulate also transitions of higher order and the coupling between them but as the contribution of the quadrupole is already very low compared to the dipole or the monpole it is most likely that these effects would lead to no visible change in the presented system.

[1] For calculation of these percentages the maximum intensity value of each image was used rather than integrating over the corresponding area. Therefore the intensities of the different images do not add up.

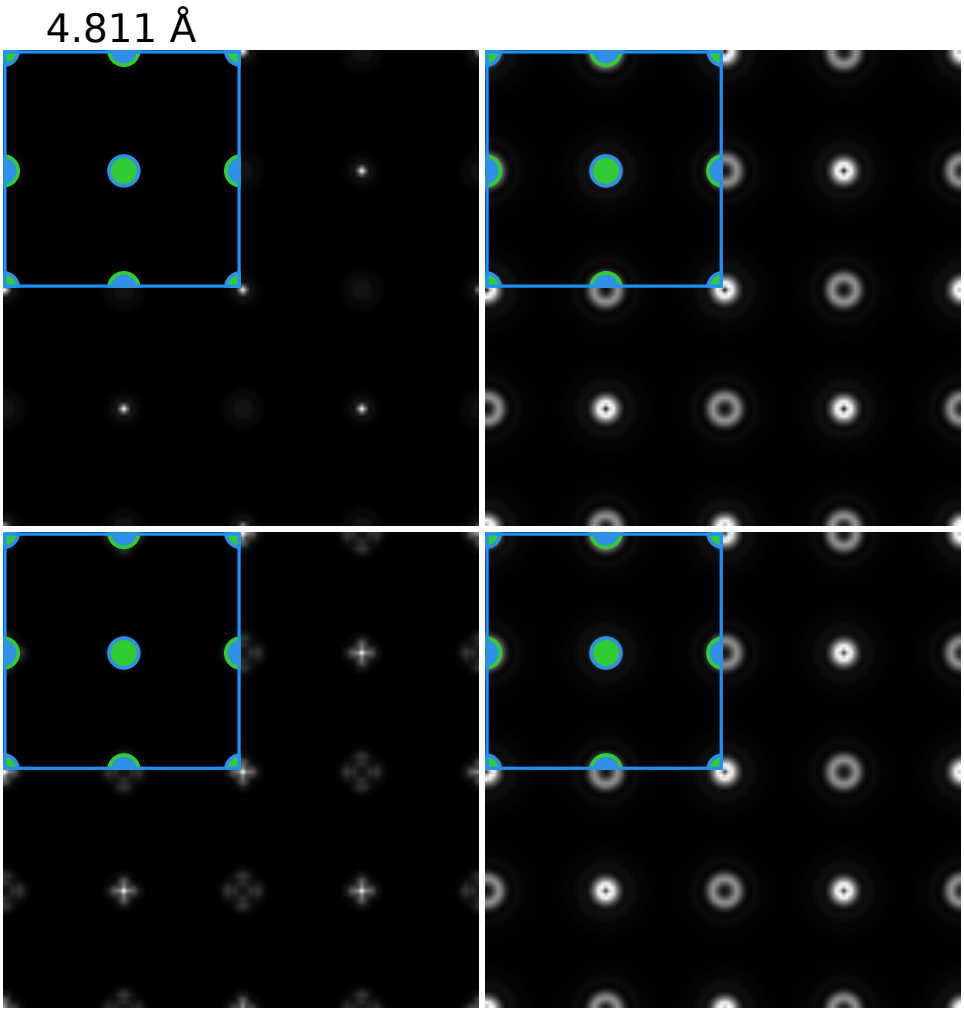

Figure 3.8: Simulation of lime in the [0 0 1] zone axis with a sample thickness of one unit cell (4.811 Å) for an energy loss of 8.8 eV above the edge onset for monopole-, dipole- and quadrupole-allowed transitions as well as for a transition in which all of these transition types are coupled (left to right, top to bottom). 200 keV incident beam energy and ideal lenses were assumed.

3.2 Rutile TiO_2

Rutile has a primitive tetragonal unit cell (see figure 3.9). Whereas the titanium atoms are surrounded by an (irregular) octahedron of six oxygen atoms, the oxygen atoms are surrounded by three titanium atoms which form a slightly distorted triangular planar system. In contrast to lime, in which the p-orbitals are equally distributed in the pDOS, this asymmetric unit cell in rutile leads to a splitting of the p-orbitals in the pDOS (see figure 3.10). This behaviour affects the scattering kernels and therefore the resulting image of a TEM investigation. For the parameter set used in the WIEN2k calculation see appendix C.

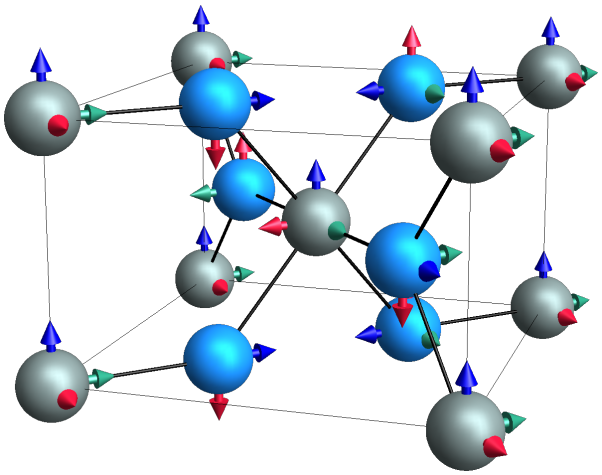

Figure 3.9: The unit cell of rutile (TiO_2). The grey balls represent the titanium atoms and the blue balls represent the oxygen atoms. The arrows represent the local coordinate systems. For details see section 2.3.

EFTEM simulations were performed for rutile with an incident beam energy of 200 keV for different zone axis geometries for the Oxygen K-edge. Depending on the energy loss as well as on the probe-to-sample orientation, different unoccupied orbitals contribute with different intensities. To elucidate the underlying physics, we first simulated a thin sample (one unit cell) and assumed ideal lenses. In order to illustrate the differences at varying energies, three energy losses (3, 4 and 7 eV above the edge onset) were chosen on the basis of the pDOS (see figure 3.10). At each energy loss different orbitals contribute: at 3 eV the pDOS for p_x, p_y and p_z have the same magnitude, at 4 eV only p_y contributes and at 7 eV p_z contributes in a large part with only a minor p_x contribution.

Figure 3.11 shows simulations for rutile in the [0 0 1] zone axis with a sample thickness of one unit cell (2.958 Å) for energy losses of 3, 4 and 7 eV above the edge onset using dipole-allowed transitions. The blue boxes

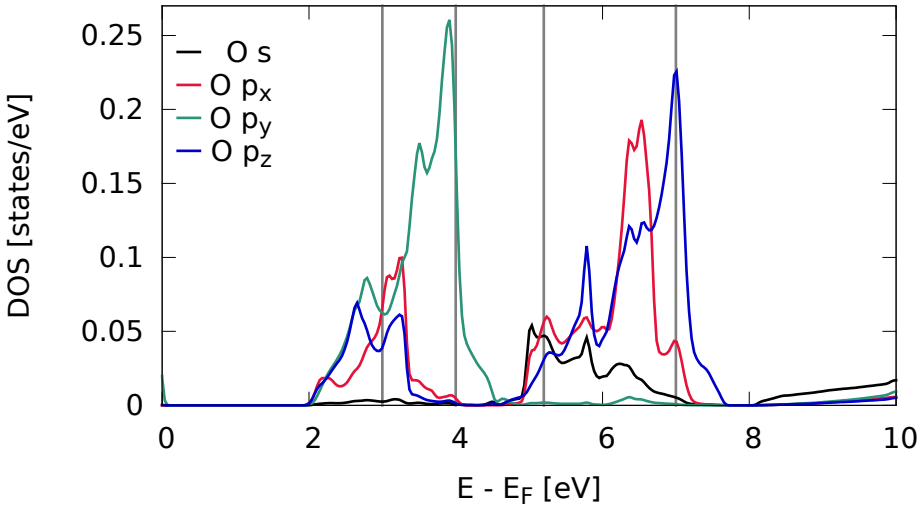

Figure 3.10: The partial DOS (pDOS) of rutile including the splitting of the p-orbital into p_x, p_y and p_z due to its distorted unit cell. The energy losses for the performed simulations are indicated at 3, 4, 5.2 and 7 eV.

in each figure show the rutile unit cell in the particular projection. Blue balls indicate oxygen atoms and grey balls titanium atoms, as already seen in figure 3.9. At 3 eV energy loss above the edge onset a mixture of p_x, p_y and p_z orbitals is seen. Therefore the shape of the overlapping orbitals cannot be compared to the dumbbell-shape of the separate p-orbitals and it resembles more a stretched ring. This ring behaviour could already be seen for the p-orbitals in lime which are degenerate (see section 3.1). At 4 eV energy loss, mostly p_y orbitals (Ti-O π^* antibonds) contribute, whereas at 7 eV, mainly the 90° rotated p_z orbitals (Ti-O σ^* antibonds) are seen. The shape of the oxygen p-orbitals and the titanium d-orbitals is indicated with the ochre/green schematic drawings.

The figures 3.12 and 3.13 show the same situation for the [1 0 0] and the [1 1 0] zone axes. As already seen for the [0 0 1] zone axis the orbitals show a circular shape due to the overlapping of the pDOS of the different orbitals for an energy loss of 3 eV above the edge onset. For an energy loss of 4 and 7 eV above the edge onset the oxygen orbitals show again the typical dumbbell shape of p-orbitals, rotated by 90° for the different energy losses. The different orientations of the orbitals for the different zone axis geometries can be explained with the orientation of the local coordinate system shown as arrows in figure 3.9. Depending on the viewing direction the arrows are pointing in different relative directions. For the [1 1 0] zone axis it seems that two of the oxygen atoms are very close, but in fact they

are in different layers of the crystal. This fact can also be seen as the orbital of one of them is more spread out than the orbital of the other oxygen atom.

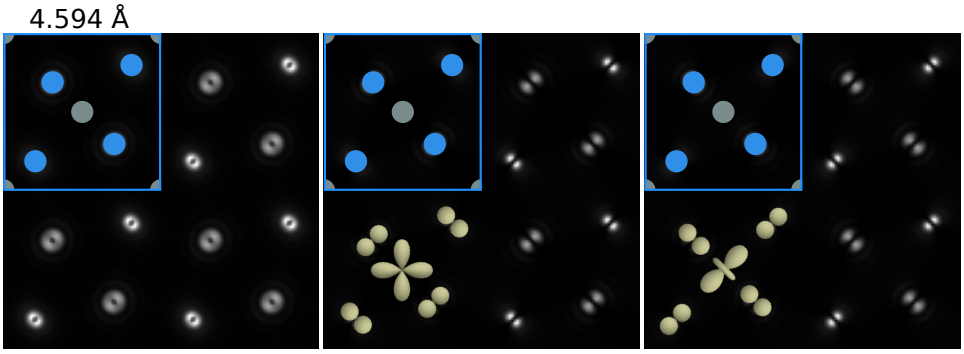

Figure 3.11: Simulation of rutile in the [0 0 1] zone axis with a sample thickness of one unit cell (2.958 Å) for energy losses of 3, 4 and 7 eV (left to right) above the edge onset for dipole-allowed transitions. 200 keV incident beam energy and ideal lenses were assumed.

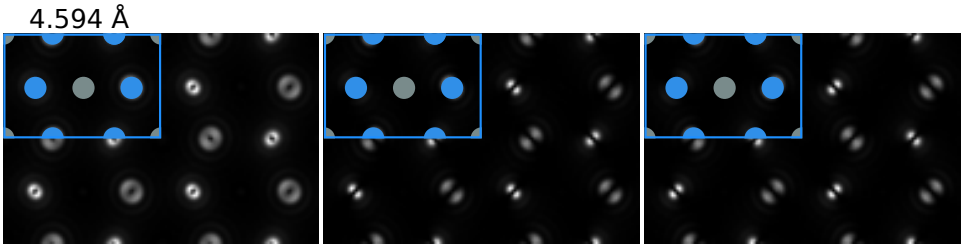

Figure 3.12: Simulation of rutile in the [1 0 0] zone axis with a sample thickness of one unit cell (2.958 Å) for energy losses of 3, 4 and 7 eV (left to right) above the edge onset for dipole-allowed transitions. 200 keV incident beam energy and ideal lenses were assumed.

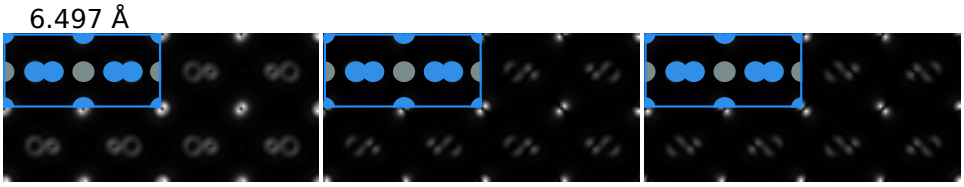

Figure 3.13: Simulation of rutile in the [1 1 0] zone axis with a sample thickness of one unit cell (2.958 Å) for energy losses of 3, 4 and 7 eV (left to right) above the edge onset for dipole-allowed transitions. 200 keV incident beam energy and ideal lenses were assumed.

3.2.1 Thickness dependence

As already mentioned for lime, it is nearly impossible in actual experiments to prepare a sample which is only one unit cell thick. Therefore we also performed simulations with more realistic thicknesses for rutile as well. Figures 3.14, 3.15 and 3.16 show a selection of the energy losses 3, 4, and 7 eV above the edge onset for the different sample orientations [1 1 0], [1 0 0] and [0 0 1], respectively, for a sample thickness of 1 unit cell, 5 nm, 10 nm and 20 nm. If the sample gets thicker, which means that the number of scattering centers increases, the electron wave for scattering events at the beginning of the sample expands and is not so localized any more, therefore the image looks blurred. Channeling effects (see also section 3.1.1) cause that from a certain sample thickness on not only the position of the oxygen atoms but also the position of the titanium atoms occur bright in the EFTEM image. For energy losses of 4 and 7 eV at which the dumbbell shape of the *p*-orbitals is clearly seen, the electron wave expands according to its symmetry along the dumbbell axis. This results in images which show a zig-zag pattern or resemble a square pattern.

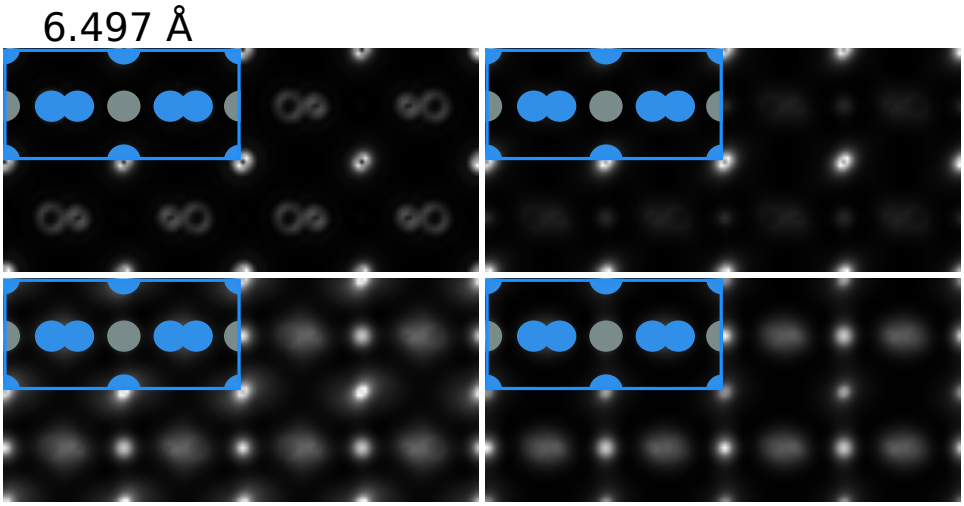

Figure 3.14: Simulation of rutile in the [1 1 0] zone axis with different sample thicknesses of 0.6497 nm (one unit cell), 5, 10 and 20 nm (left to right, top to bottom) for an energy loss of 3 eV above the edge onset for dipole-allowed transitions. 200 keV incident beam energy and ideal lenses were assumed.

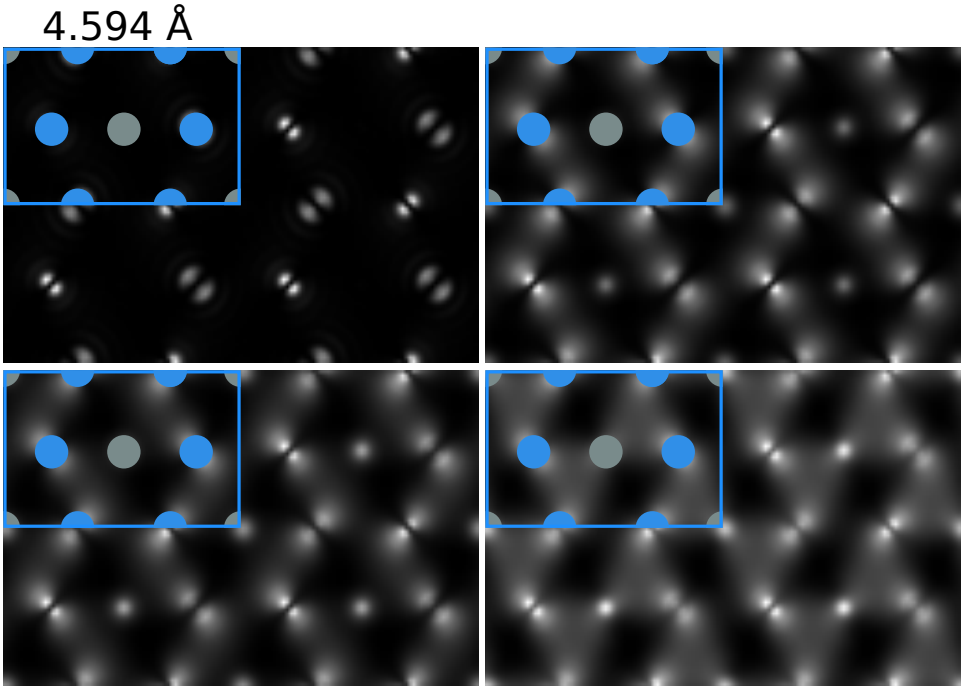

Figure 3.15: Simulation of rutile in the [1 0 0] zone axis with different sample thicknesses of 0.4594 nm (one unit cell), 5, 10 and 20 nm (left to right, top to bottom) for an energy loss of 4 eV above the edge onset for dipole-allowed transitions. 200 keV incident beam energy and ideal lenses were assumed.

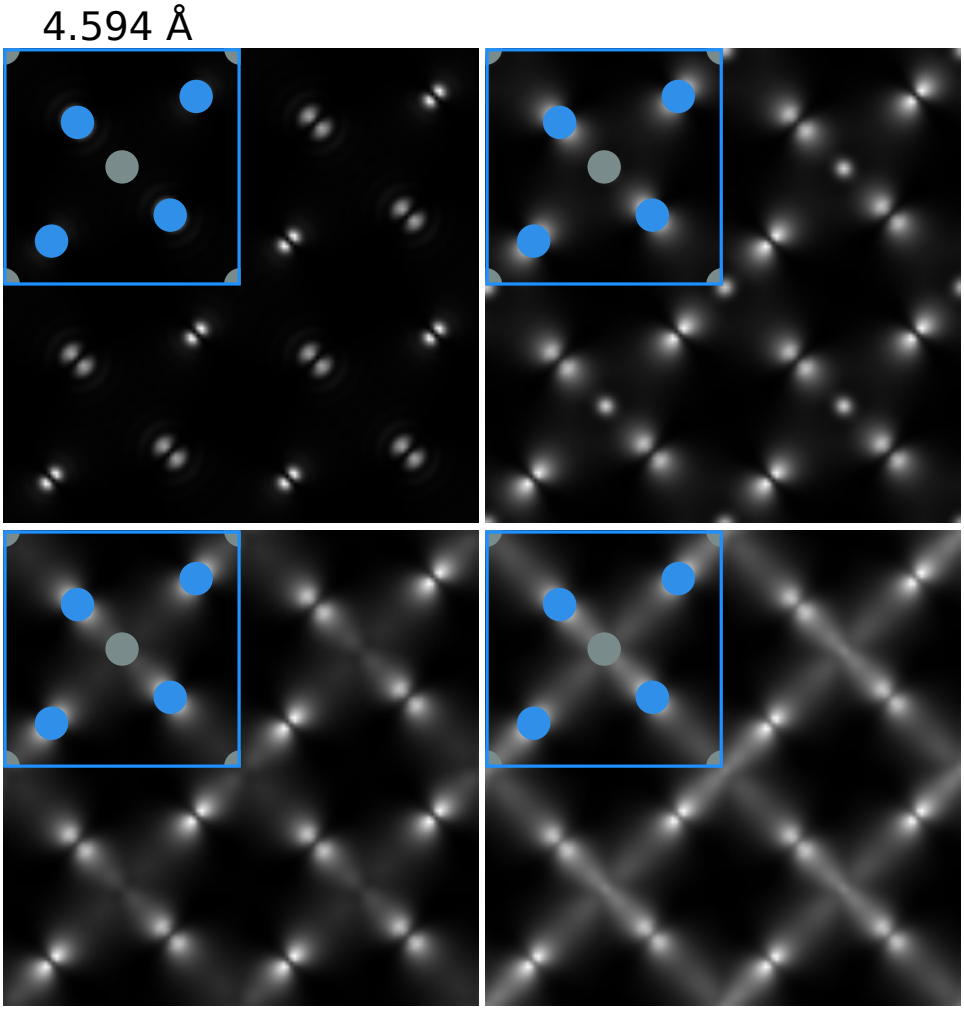

Figure 3.16: Simulation of rutile in the [0 0 1] zone axis with different sample thicknesses of 0.2958 nm (one unit cell), 5, 10 and 20 nm (left to right, top to bottom) for an energy loss of 7 eV above the edge onset for dipole-allowed transitions. 200 keV incident beam energy and ideal lenses were assumed.

3.2.2 Aberrations

Again we take a step further and perform simulation with realistic values for the lens system instead of assuming a set of ideal lenses. Figures 3.17, 3.18 and 3.19 show a comparison of the three different sets of lens parameters given in table 3.1 for selected energy losses and orientations. In each of these figures it can again be seen that in a Tecnai microscope the atoms are dark whereas for a set of ideal lenses or in a Titan microscope the atoms appear bright. This is due to the sign change in the transfer function (see section 3.1.2 for details). It is evident that the images simulated with lens parameters like in a Titan microscope look similar to the ideal images. That means the orbital shape is spread and blurred but each atomic position can still be identified. This is not so easy for images simulated with the lens paramters of a Tecnai microscope. For these parameters it is hard to identify the atomic position and no orbital shapes can be made out. In real experiments both effects – the lens errors as well as the sample thickness – have significant influence on the resulting images. Therefore simulations for thicker samples with different parameters for the lens system were performed. Figure 3.20 shows a comparison of the thickness dependence (5, 10 and 20 nm) with three different sets of the lens parameters (see table 3.1). For an imaging system like in a Tecnai microscope no orbital shapes can be made out and as the sample gets thicker it is hard to recognize the atomic positions. On the other hand, for an imaging system as in a Titan microscope even for thick sample it is still possible to recognize the atomic positions and the orbital shapes. With these realistic values comparisons with experiments are possible.

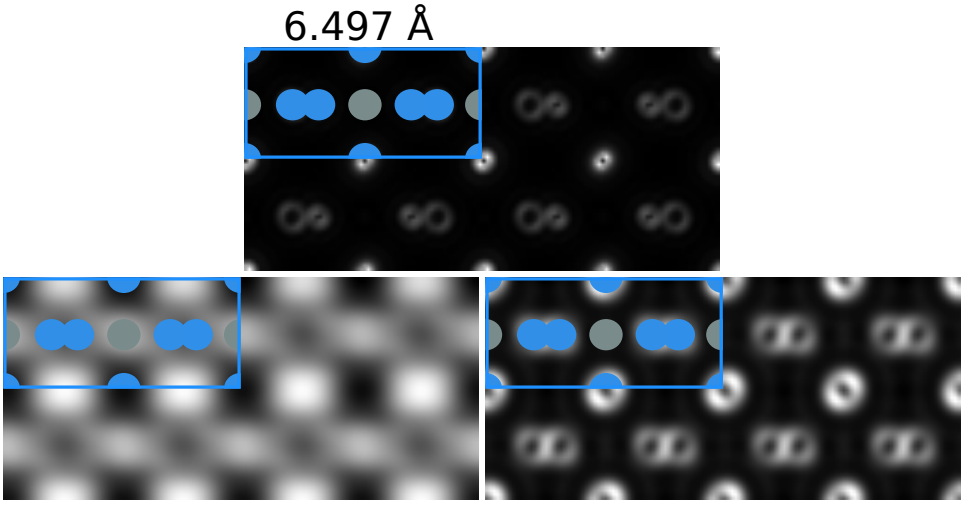

Figure 3.17: Simulation of rutile in the [1 1 0] zone axis with a sample thickness of one unit cell (6.497 Å) for an energy loss of 3 eV above the edge onset for dipole-allowed transitions. 200 keV incident beam energy and three different parameters sets for the lens system (see table 3.1) were assumed: Ideal lenses (top), lenses as in a Tecnai microscope (bottom, left) and lenses as in a Titan microscope (bottom, right).

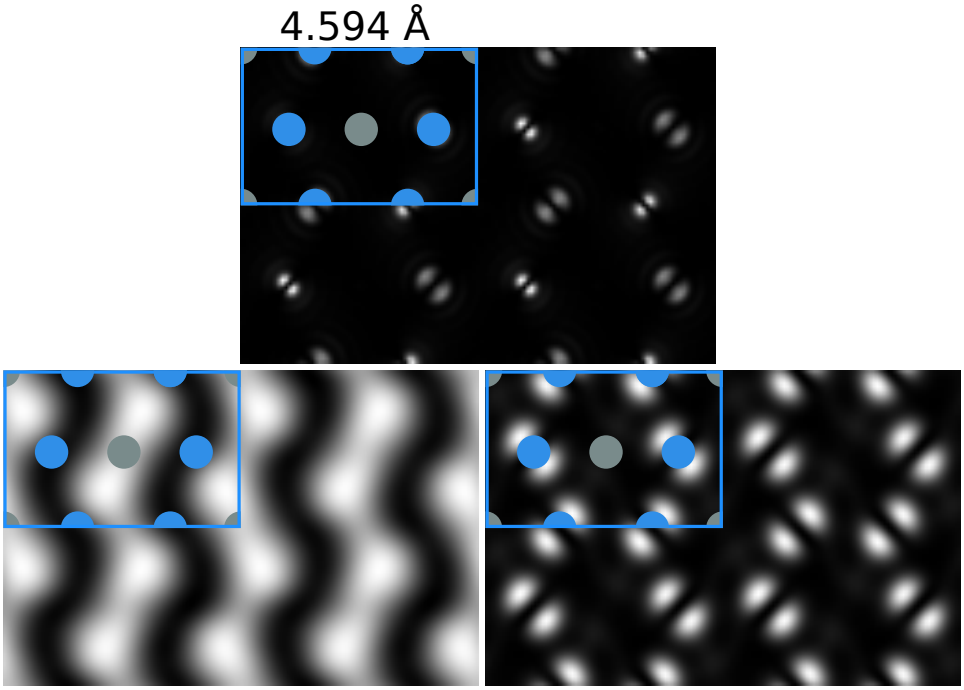

Figure 3.18: Simulation of rutile in the [1 0 0] zone axis with a sample thickness of one unit cell (4.594 Å) for an energy loss of 4 eV above the edge onset for dipole-allowed transitions. 200 keV incident beam energy and three different parameters sets for the lens system (see table 3.1) were assumed: Ideal lenses (top), lenses as in a Tecnai microscope (bottom, left) and lenses as in a Titan microscope (bottom, right).

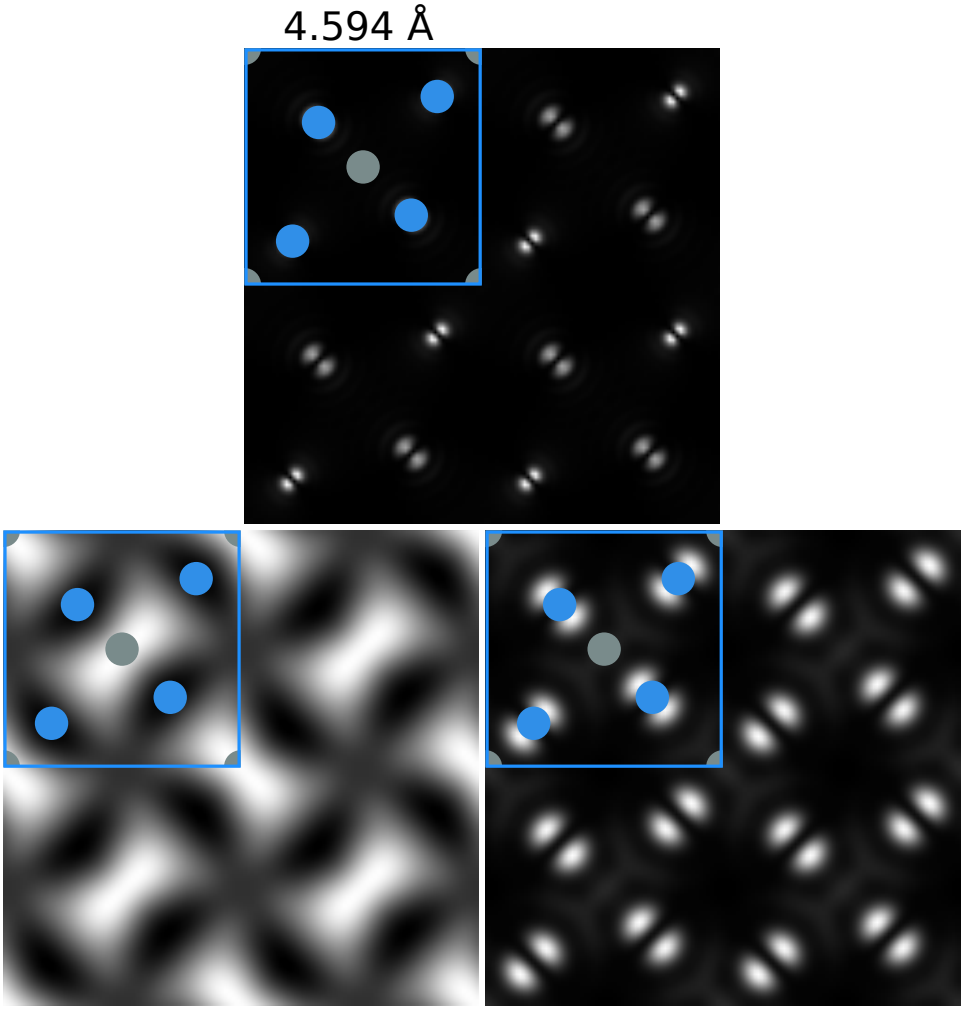

Figure 3.19: Simulation of rutile in the [0 0 1] zone axis with a sample thickness of one unit cell (2.958 Å) for an energy loss of 7 eV above the edge onset for dipole-allowed transitions. 200 keV incident beam energy and three different parameters sets for the lens system (see table 3.1) were assumed: Ideal lenses (top), lenses as in a Tecnai microscope (bottom, left) and lenses as in a Titan microscope (bottom, right).

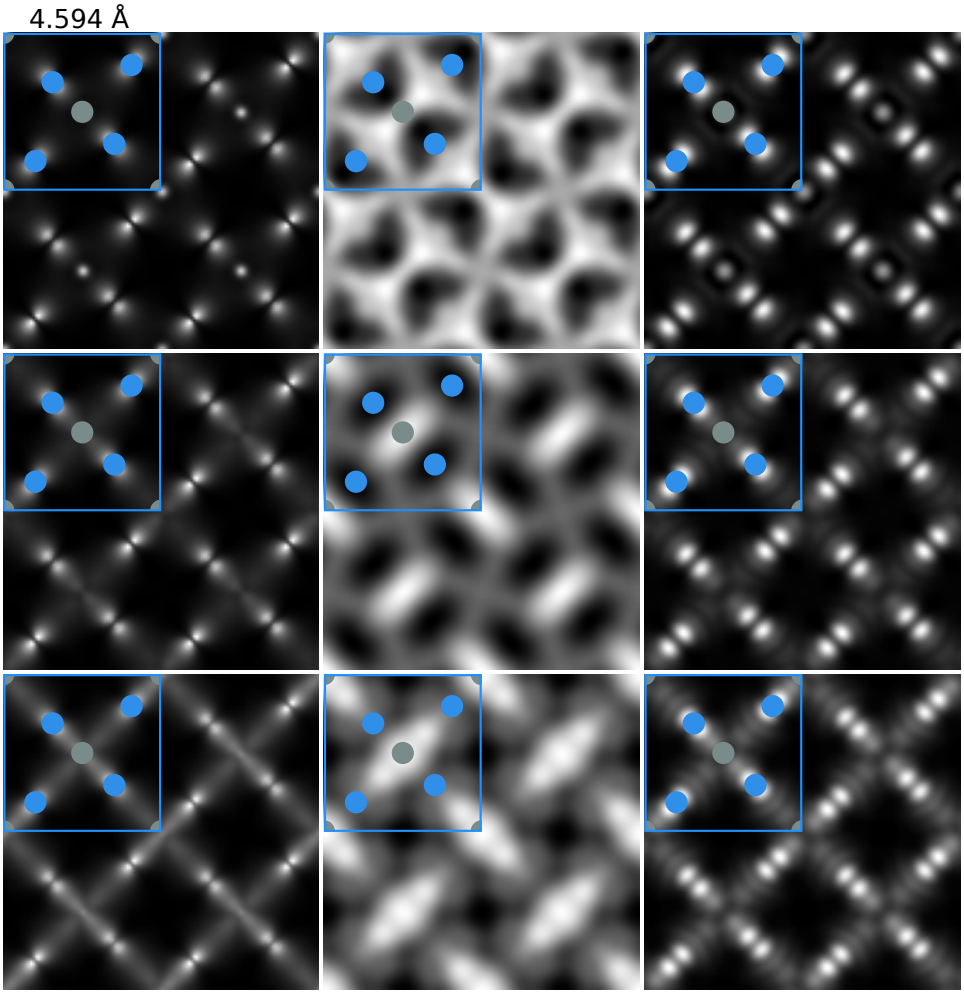

Figure 3.20: Simulation of rutile in the [0 0 1] zone axis with different sample thicknesses of 5, 10 and 20 nm (top to bottom) for an energy loss of 7 eV above the edge onset for dipole-allowed transitions. 200 keV incident beam energy and three different parameters sets for the lens system (see table 3.1) were assumed: Ideal lenses (left column), lenses as in a Tecnai microscope (middle column) and lenses as in a Titan microscope (right column).

3.2.3 Multipole coupling

Instead of looking only at dipole-allowed transitions, we also performed calculations taking into account the coupling between different transition types. In contrast to the multipole calculations for lime, we only coupled monopole- and dipole-allowed transitions. An energy loss of 5.2 eV above the edge onset was chosen (as indicate in figure 3.10) because at this particular energy loss the s-orbital as well as the p_x- and the p_z-orbitals contribute. If the orbitals at a specific energy loss are not overlapping in the pDOS no coupling term occurs. Therefore the energy loss has to be chosen wisely to demonstrate the multipole coupling. A comparison of EFTEM images of a monopole- and a dipole-allowed transition as well as a calculation taking both monopole and dipole into account is shown in figure 3.21. The green framed image shows the monopole-allowed transition. It displays a circular symmetry as expected for an s-orbital. For the dipole transition (blue frame) an overlapping of the p_x- and the p_z-orbitals is seen. This result in an orbital which resembles a blurred dumbbell. Calculations including monopole and dipole transitions at the same time (red frame) look similar to the dipole transition-only image. In order to analyse the differences we subtracted the intensity of the monopole transition and of the dipole transition from the intensity of the image when both transition types are taken into account.

$$I_{coupling} = I_{\lambda=0,1} - I_{\lambda=0} - I_{\lambda=1} \tag{3.2}$$

The resulting coupling term is also shown in figure 3.21 in the grey frame. Intensity profiles along the yellow lines are shown in the bottom of figure 3.21 demonstrating that the coupling term has significant impact. From this intensity profiles it can be explained why the coupled transition image and the dipole transition image look so similar. If we normalize the intensity of the dipole-allowed transition to 100% then the coupled transition yields 105.4%. The monopole transition (8.6%) only plays a minor role. But in contrast to lime in which the coupling term had no significant influence (of the order of 0.0001%) the situation is completely different for rutile. In this material the coupling term accounts for $\pm$9.0% of the total intensity. Further examination of the intensity profile shows that the coupling term is distributed asymmetrical around the origin. This acts in a way very similar to s-p hybridization.

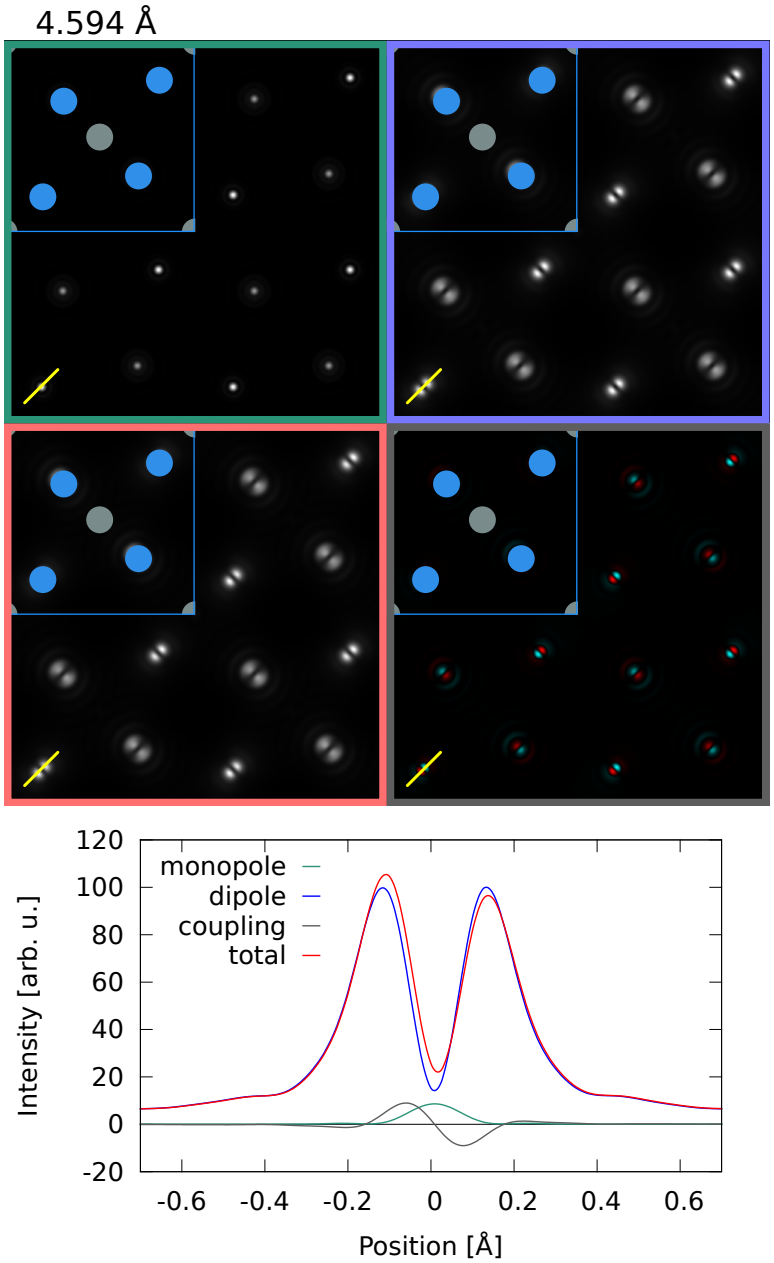

Figure 3.21: Simulation of rutile in the [0 0 1] zone axis with a sample thickness of one unit cell (2.958 Å) for an energy loss of 5.2 eV above the edge onsetfor a monopole transition (green), a dipole transition (blue) and the coupling between them (grey) together with the total intensity (red). 200 keV incident beam energy and ideal lenses were assumed. The colour of the coupling term indicates its sign. The bottom image of this figure shows the intensity profiles along the yellow lines in which the line color matches the frame color from the upper images.

Chapter 4

Conclusion and outlook

It was demonstrated how the MDFF can be diagonalized using matrix diagonalization techniques. This simpler mathematical description of the system yields numerical advantages as the number of terms is reduced. With the default settings of WIEN2k, the number of terms was reduced from up to 1296 terms to at most 36 terms. Further, this transformation into the most suitable basis set to describe a system provides us with more physical insight into the problem.

This new simulation method was applied to lime (CaO) and rutile (TiO_2) in order to show its versatility. From the EFTEM simulations of these materials it can be seen that with the latest generations of TEMs orbital mapping should be possible.

Calculations including transition types of both dipole-allowed and dipole-forbidden can be performed. Although commonly neglected, we also include non-dipole transitions in our simulation. It can be seen that also the monopole and particularly the coupling term between different transition types can have significant impact on the resulting EFTEM images, especially in rutile.

Because in low-symmetry systems a splitting of the pDOS is expected, mapping of orbital information should be possible in those cases. In the future, this method could be applied to study the electronic structure of defects, interfaces, or other low-symmetry objects.

Appendix A

Hermiticity of the XDOS

According to equation 1.20 the XDOS reads

$$X_{LM_LL'M'_L} = \sum_{\mathbf{k}n} D^{\boldsymbol{k}n}_{LM_L} (D^{\boldsymbol{k}n}_{L'M'_L})^* \delta(E + E_{nlj} - E_{\mathbf{k}n}). \tag{A.1}$$

In order to be hermitian, the XDOS has to fullfill

$$X_{LM_LL'M'_L} = (X_{L'M'_LLM_L})^*. \tag{A.2}$$

$$\begin{aligned}
(X_{L'M'_LLM_L})^* &= \left(\sum_{\mathbf{k}n} D^{\boldsymbol{k}n}_{L'M'_L} (D^{\boldsymbol{k}n}_{LM_L})^* \delta(E + E_{nlj} - E_{\mathbf{k}n}) \right)^* \\
&= \sum_{\mathbf{k}n} (D^{\boldsymbol{k}n}_{L'M'_L})^* D^{\boldsymbol{k}n}_{LM_L} \delta(E + E_{nlj} - E_{\mathbf{k}n}) \\
&= \sum_{\mathbf{k}n} D^{\boldsymbol{k}n}_{LM_L} (D^{\boldsymbol{k}n}_{L'M'_L})^* \delta(E + E_{nlj} - E_{\mathbf{k}n}) \\
&= X_{LM_LL'M'_L}
\end{aligned} \tag{A.3}$$

Appendix B

Hermiticity of Ξ

For $\boldsymbol{\Xi}$ to be hermitian, the following condition has to hold.

$$\Xi_{\alpha'\alpha} = {\Xi_{\alpha'\alpha}}^{\dagger} = {\Xi_{\alpha\alpha'}}^{*} \tag{B.1}$$

$$\begin{aligned}
\Xi_{\alpha\alpha'} =& 2 \sum_{M_L M_L'} 4\pi(-1)^{L+L'}(2l+1)\sqrt{[\lambda,\lambda',L,L']} \\
& \begin{pmatrix} l & \lambda & L \\ 0 & 0 & 0 \end{pmatrix} \begin{pmatrix} l & \lambda' & L' \\ 0 & 0 & 0 \end{pmatrix} \sum_{m_l} \begin{pmatrix} l & \lambda & L \\ -m_l & \mu & M_L \end{pmatrix} \begin{pmatrix} l & \lambda' & L' \\ -m_l & \mu' & M_L' \end{pmatrix} \\
& i^{\lambda-\lambda'} \sum_{\mathbf{k}n} D^{\boldsymbol{k}n}_{LM_L} (D^{\boldsymbol{k}n}_{L'M_L'})^* \delta(E + E_{nlj} - E_{\mathbf{k}n})
\end{aligned} \tag{B.2}$$

$$\begin{aligned}
\Xi_{\alpha'\alpha} =& 2 \sum_{M_L' M_L} 4\pi(-1)^{L'+L}(2l+1)\sqrt{[\lambda',\lambda,L',L]} \\
& \begin{pmatrix} l & \lambda' & L' \\ 0 & 0 & 0 \end{pmatrix} \begin{pmatrix} l & \lambda & L \\ 0 & 0 & 0 \end{pmatrix} \sum_{m_l} \begin{pmatrix} l & \lambda' & L' \\ -m_l & \mu' & M_L' \end{pmatrix} \begin{pmatrix} l & \lambda & L \\ -m_l & \mu & M_L \end{pmatrix} \\
& i^{\lambda'-\lambda} \sum_{\mathbf{k}n} D^{\boldsymbol{k}n}_{L'M_L'} (D^{\boldsymbol{k}n}_{LM_L})^* \delta(E + E_{nlj} - E_{\mathbf{k}n}) \\
=& 2 \sum_{M_L M_L'} 4\pi(-1)^{L+L'}(2l+1)\sqrt{[\lambda,\lambda',L,L']} \\
& \begin{pmatrix} l & \lambda & L \\ 0 & 0 & 0 \end{pmatrix} \begin{pmatrix} l & \lambda' & L' \\ 0 & 0 & 0 \end{pmatrix} \sum_{m_l} \begin{pmatrix} l & \lambda & L \\ -m_l & \mu & M_L \end{pmatrix} \begin{pmatrix} l & \lambda' & L' \\ -m_l & \mu' & M_L' \end{pmatrix} \\
& \left[i^{\lambda-\lambda'} \sum_{\mathbf{k}n} D^{\boldsymbol{k}n}_{LM_L} (D^{\boldsymbol{k}n}_{L'M_L'})^* \delta(E + E_{nlj} - E_{\mathbf{k}n}) \right]^* \\
=& {\Xi_{\alpha\alpha'}}^{*}
\end{aligned} \tag{B.3}$$

Appendix C

WIEN2k parameters

Lattice spacegroup	225 Fm-3m
Lattice parameters	$a = b = c = 4.811$ Å $\alpha = \beta = \gamma = 90°$
Ca position	(0,0,0)
O position	(0.5,0.5,0.5)
Exchange correlation potential	PBE-GGA (Perdew-Burke-Ernzerhof 96)
$R_{mt}K_{max}$	7
Number of k-points	1000

Table C.1: Input parameters for WIEN2k to calculate the pDOS of lime.

Lattice spacegroup	136 P42/mnm
Lattice parameters	$a = b = 4.594$ Å, $c = 2.958$ Å $\alpha = \beta = \gamma = 90°$
Ti positions	(0,0,0) (0.5,0.5,0.5)
O positions	(0.3053,0.3053,0) (0.6947,0.6947,0) (0.1947,0.8053,0.5) (0.8053,0.1947,0.5)
Exchange correlation potential	PBE-GGA (Perdew-Burke-Ernzerhof 96)
$R_{mt}K_{max}$	7
Number of k-points	1000

Table C.2: Input parameters for WIEN2k to calculate the pDOS of rutile.

Bibliography

[1] P. Schattschneider, M. Nelhiebel, M. Souchay, and B. Jouffrey. The physical significance of the mixed dynamic form factor. *Micron*, 31:333–345, 2000.

[2] S. Löffler, I. Ennen, F. Tian, P. Schattschneider, and N. Jaouen. Breakdown of the dipole approximation in core losses. *Ultramicroscopy*, 111(8):1163 – 1167, 2011.

[3] P. Schattschneider, M. Stöger-Pollach, and W. Werner. Electron beam techniques for nanoanalysis, 2011. Lecture notes.

[4] R. F. Egerton. Electron energy-loss spectroscopy in the TEM. *Reports on Progress in Physics*, 72(1):016502, 2009.

[5] D.B. Williams and C.B. Carter. *Transmission Electron Microscopy: A Textbook for Materials Science*. Number Bd. 1 in Transmission Electron Microscopy: A Textbook for Materials Science. Plenum Press, 1996.

[6] Wikimedia Commons. Scheme TEM en, 2012. [Online; accessed 26-September-2012].

[7] E.J. Kirkland. *Advanced Computing in Electron Microscopy*. SpringerLink: Springer e-Books. Springer, 2010.

[8] M. Zauner. Multislice approach for high resolution energy filtered inelastic image simulation. Master's thesis, TU Wien, 2010.

[9] S. L. Dudarev, L.-M. Peng, and M. J. Whelan. Correlations in space and time and dynamical diffraction of high-energy electrons by crystals. *Phys. Rev. B*, 48:13408–13429, Nov 1993.

[10] K. Blum. *Density Matrix Theory And Applications*. Plenum Press, 1996.

[11] C. Cohen-Tannoudji, B. Diu, and F. Laloë. *Quantum mechanics*. Wiley, 1977.

[12] M. Nelhiebel. *Effects of crystal orientation and interferometry in electron energy loss spectroscopy.* PhD thesis, École Centrale Paris, 1999.

[13] H. Kohl and H. Rose. Theory of image formation by inelastically scattered electrons in the electron microscope. volume 65 of *Advances in Electronics and Electron Physics*, pages 173 – 227. Academic Press, 1985.

[14] P. Schattschneider. *Fundamentals of inelastic electron scattering.* Springer-Verlag, 1986.

[15] S. Löffler, V. Motsch, and P. Schattschneider. A factorization approach of the mixed dynamic form factor for mapping atomic orbitals. submitted to Ultramicroscopy.

[16] P. Schattschneider, M. Nelhiebel, and B. Jouffrey. Density matrix of inelastically scattered fast electrons. *Phys. Rev. B*, 59:10959–10969, 1999.

[17] Wikipedia. Quadratic form — Wikipedia, the free encyclopedia, 2012. [Online; accessed 24-October-2012].

[18] P. Blaha, K. Schwarz, G. Madsen, D. Kvasnicka, and J. Luitz. *WIEN2k, An Augmented Plane Wave + Local Orbitals Program for Calculating Crystal Properties.* Karlheinz Schwarz, Techn. Universität Wien, Austria, 2001. ISBN 3-9501031-1-2.

[19] K. Jorissen. *The ab initio calculation of relativistic electron energy loss spectra.* PhD thesis, Universiteit Antwerpen, 2007.

[20] Stefan Löffler and Peter Schattschneider. Transition probability functions for applications of inelastic electron scattering. *Micron*, 43(9):971 – 977, 2012.

[21] Wikimedia Commons. Euler angles, 2012. [Online; accessed 14-June-2012].

[22] Wikipedia. Wigner d-matrix — Wikipedia, the free encyclopedia, 2012. [Online; accessed 11-June-2012].

[23] Wikipedia. Schur decomposition — Wikipedia, the free encyclopedia, 2012. [Online; accessed 22-May-2012].